5 Radiation Sources

This chapter describes the radiation sources to be provided in the NSLS-II baseline configuration. Continuing the tradition established by the existing NSLS, they span a very wide spectral range, from the far IR, down to 0.1 meV (equivalent to 1 cm^{-1}), to the very hard x-ray region, more than 300 keV. This is achieved by a combination of bending magnet sources, covering the IR, VUV, and soft x-ray range, three-pole wiggler sources extending into the hard x-ray range, and insertion device sources, covering the soft x-ray through very hard x-ray range. They will achieve world leading levels of time average brightness and flux from the far IR through to ~20 keV, only being surpassed above ~20 to 25 keV by the performance of synchrotrons operating at higher energy (6 to 8 GeV).

As discussed in elsewhere in this report, the NSLS-II lattice contains 30 DBA cells, or 15 superperiods with alternating straight section lengths. The beta function values at the centers of the shorter straight sections will be quite low, especially in the vertical plane, and the longer straights will have somewhat higher beta function values. The resulting horizontal and vertical electron beam sizes and divergences in the center of the two types of straights, as well as in the center of the bend magnets and three-pole wigglers, are given in Table 5.1.1. These beam sizes and divergences are very small, especially in the insertion device straight sections. The beta functions also determine the allowed minimum vertical gap of an undulator and non-linear dynamic effects constrain the maximum length of the undulator, L. The minimum undulator gap and the undulator lengths for the devices described in this chapter were all chosen to satisfy these constraints.

All of the source properties described in this chapter assume a fully-damped horizontal emittance value of 0.5 nm-rad. This is the performance value for the NSLS-II storage ring when operating with a full complement of eight 7 m damping wigglers. The initial emittance value will be greater than this value, owing to operation with fewer damping wigglers, as discussed in Chapter [xx].

Table 5.1.1 Electron Beam Size and Divergence at NSLS-II.

Type of source	Low- straight section (6.6m)	High- straight section (8.6m)	0.4T Bend magnet	1T three-pole wiggler
σ_h [μm]	28.	99.5	44.2 (35.4-122)	136
σ_h' [μrad]	19.	5.5	63.1 (28.9 – 101)	14.0
σ_v [μm]	2.6	5.5	15.7	15.7
σ_v' [μrad]	3.2	1.8	0.63	0.62

5.1 Insertion Devices

The goal in choosing the set of principal insertion device parameters is to provide a wide overall spectral coverage with insertion devices that target the photon energy ranges of interest for the experimental programs. It is expected that other parameter choices besides those outlined here may be specified to meet the needs of the science program as it evolves over time.

The set of insertion devices described included in the baseline configuration of NSLS-II consists of hard x-ray and soft x-ray undulators, x-ray damping wigglers, and high-energy superconducting wigglers. Their spectral brightness, flux, power, spatial and angular output properties, and polarization performance are described. These IDs produce high-brightness radiation spanning a large photon energy range, from the soft x-ray (~200 eV) to the very hard x-ray (~300 keV). An R&D program focused on developing the required magnetic and mechanical design of these devices is presented in Chapter [xx]. Their effects on the properties of the NSLS-II storage ring and other accelerator physics issues are presented in Chapter [xx].

Table 5.1.2: Insertion Devices included in the Baseline Configuration of NSLS-II

Type of Device	Purpose	Usage	Quantity
Damping Wiggler: 90 mm period (DW90), 1.8T, 2 × 3.5-m long	Broadband	Machine/User	3
In-Vacuum Undulator (IVU): 20mm period (U20), 1.81T, 3-m long	Hard X-ray	User	3
Elliptically-polarized undulator (EPU): 45mm period (EPU45), 4.33T, 2 × 2-m long, canted by ~0.25 mrad	Soft X-ray	User	1
Three-Pole Wiggler: 1.0T, 20cm long	Broadband	User	≤15

The complement of insertion devices included in the NSLS-II baseline configuration is listed in Table 5.1.2. This set is not meant to be complete for the built-out NSLS-II facility. Rather, these devices represent a set that attempts to optimize the performance of the beamlines included in the NSLS-II baseline configuration. These IDs have been chosen consistent with the philosophy of building beamlines dedicated to a given technique, which requires that the source also be individually optimized for each application, as appropriate.

[[remove paragraph?? Other types of undulators and/or wigglers besides those discussed in this Chapter will also be considered during the preliminary engineering design phase of the project. These will include in-vacuum EPUs, to reach smaller magnetic gaps and thereby cover wider photon energy ranges, and quasi-periodicity, for both planar undulators and EPUs. In addition, revolver concepts, figure-8 type undulators, and long-period electromagnetic undulators will be considered. These concepts are discussed further in the description of the undulator R&D program in Chapter 12.]]

5.1.1 Planar Undulators

The hard x-ray undulators at NSLS-II will be planar designs and will produce linearly polarized radiation.

5.1.1.1 IVU – U20

The baseline NSLS-II hard x-ray undulator is an In-Vacuum Undulator (IVU) with a period of 20 mm, referred to as U20. This device will be operated at room temperature and is based on the mini-gap in-vacuum undulator design and development pioneered at NSLS and now utilized at SR sources around the world.

5.1.2 Elliptically Polarized Undulators

The NSLS-II soft x-ray insertion devices will be elliptically-polarized undulators. EPUs provide full ellipticity control of the radiated output from circular through linear, while only marginally reducing the brightness of the linearly polarized output, compared to pure planar undulators of the same period. In addition, these EPUs can also provide linearly polarized output with the polarization axis oriented either horizontally, vertically, or anywhere in between. As discussed in the soft x-ray beamline Section [xx], these properties are extremely useful for separating various contributions to a given signal in an experiment.

5.1.2.1 Soft X-ray EPU – EPU45

The total length of the EPU45 undulator is specified as 4 m, corresponding to a single long device. However, this corresponds to only one of two proposed operating modes for these devices. In fact, for the soft x-ray beamlines discussed in Chapter [xx], this 4 m total length would be comprised of two ~2 m EPUs and the appropriate steering magnets and diagnostics would be placed between the sections to allow a small (~0.25 mrad) canting angle for the electron beam between them. As described in more detail in Chapter [xx],

this configuration will allow the two undulator sections to be set to two different polarizations, e.g., left circular and right circular, or horizontal linear and vertical linear. The angular separation provided by the canting will then permit fast switching between the chosen polarizations of the two EPUs, thereby enabling various types of polarization-sensitive experiments to be performed with high sensitivity, as provided by lock-in detection methods for example. The accelerator issues associated with these, and other, canting angles are discussed briefly in Section [xx] and will be addressed in more detail in the technical design phase of this project.

5.1.3 Wigglers

Classes of experiments that require continuous x-ray spectra, sizable x-ray beams, or very hard x-rays, such as EXAFS, powder diffraction, x-ray topography, x-ray standing waves, high pressure, and x-ray footprinting, to name some, will benefit from the availability of x-ray beamlines that view damping wiggler sources. Superconducting wigglers will be the preferred source for experiments requiring very hard x-rays, up to ~300 keV. All wiggler sources at NSLS-II are expected to be in high demand.

5.1.3.1 Damping Wiggler – DW90

The damping wigglers will produce the highest flux of any NSLS-II source out to ~30 keV and will also have excellent brightness. They are expected to be the premier source for experiments above ~5 keV that do not require the ultra-high brightness and extremely small beams produced by the hard x-ray undulators.

5.1.3.2 Three-pole Wiggler – TPW

The three-pole wigglers, to be inserted just upstream of the downstream bend magnet in the super-period, will produce a very useful hard x-ray bend-magnet-like spectrum. With a critical energy of 6 keV, the three-pole wigglers will produce usable hard x-ray flux out to ~25 keV. The emitted horizontal angular fan from these devices is 2 mrad wide.

5.1.3.3 Superconducting Wiggler – SCW60

The highest energy photons will be produced by very high field, short period, wigglers. The radiation will be broadband with high power at high x-ray energies, covering the 20 to 300 keV energy range. The baseline SCW60 device has a period length of 60mm and a wiggler field of 3.5T. This combination of period and magnetic field has been demonstrated technologically at ELETTRA and MAX lab. Specifications of other high magnetic field SCWs that are currently in service at medium energy synchrotrons are listed in Table 5.1.3.

Table 5.1.3 Some Working SCWs Similar in Specifications to Proposed and Alternative NSLS-II Wigglers.

Facility	Manufacturer	Field(T)	Period (cm)	# full-field poles
NSLS X17	Oxford	6	17.4	5
BESSY II	Novosibirsk	7	14.8	13
CLS	Novosibirsk	4.2	4.8	25
ELETTRA	Novosibirsk	3.6	6.4	45
MAX lab	Custom	3.5	6.1	47

Increasing the SCW60 magnetic field will be the subject of NSLS-II R&D, so that its flux and brightness are as high as possible. A target magnetic field value is 6.0T, which represents an SCW design that pushes the limit of presently achievable current density. The SCW60 will outperform other NSLS-II radiation sources at

energies above 30 keV. The target deflection parameter, K, is chosen to be high enough to generate a large horizontal beam profile of more than 0.5 m at 50 m from the source point. This allows splitting of the fan into multiple experimental hutches.

5.2 Bend Magnets

The NSLS-II bending magnets will have a relatively low critical energy (2.4 keV), and will be excellent sources for low photon energies, below 10 keV. It is expected that the available bend magnet ports will be allocated primarily to VUV and soft x-ray uses, as well as infrared uses. Those classes of experiments that require access to harder sources of bend-magnet-like x-rays (energy >~5 keV) are better suited to three-pole wigglers (TPW), described in section 5.1.3.2 above.

The NSLS-II bend magnets and three-pole wigglers will provide very stable beams. The relatively low emitted power from these sources simplifies the cooling requirements on the optics, although it does not eliminate the need to provide cooling. The brightness provided by the NSLS-II dipole sources will be two orders of magnitude higher than that of the present NSLS dipoles (extending up to ~12 keV) and their flux will also show some improvement (extending up to ~4 keV), as shown in Table 5.2.1. Indeed, the NSLS-II bend magnets will provide almost twice the flux of the ALS conventional bend magnets (i.e., not the superbends) and offer even larger improvements in source brightness. Thus, aspects of the very successful ALS research programs based on bend magnet illumination can be developed at NSLS-II, although the distribution of beamlines and end stations will be determined by the strengths and interests of the NSLS-II user community. The NSLS-II 3 three-pole wiggler sources will have essentially the same critical energy as the present NSLS dipoles, but will be more than an order of magnitude brighter and produce a factor of 1.5 to 3 times greater flux (see Table 5.2.1).

Table 5.2.1 Comparison of Bend Magnet Sources

	NSLS-II Bend Magnet		NSLS-II Three-pole-wiggler		ALS Conventional Bend Magnet		NSLS X-Ray Bend Magnet		NSLS VUV Bend Magnet	
Energy	Flux	Brightness	Flux	Brightness	Flux	Brightness	Flux	Brightness	Flux	Brightness
1000 eV	3.3×10^{13}	1.5×10^{16}	3.3×10^{13}	2.7×10^{16}	2.1×10^{13}	1.5×10^{15}	1.4×10^{13}	1.3×10^{14}	6.0×10^{12}	1.1×10^{13}
100 eV	2.5×10^{13}	8.0×10^{15}	1.9×10^{13}	1.3×10^{15}	1.5×10^{13}	7.5×10^{14}	8.0×10^{12}	7.0×10^{13}	1.3×10^{13}	9.0×10^{13}
10 eV	1.3×10^{13}	3.7×10^{15}	9.3×10^{12}	6.0×10^{14}	7.2×10^{12}	3.4×10^{14}	3.8×10^{12}	2.8×10^{13}	7.7×10^{12}	4.4×10^{12}
1 eV	5.9×10^{12}	1.7×10^{15}			3.4×10^{12}	1.6×10^{14}	1.8×10^{12}	1.3×10^{13}	3.7×10^{12}	2.0×10^{12}
0.1 eV	2.8×10^{12}	8.0×10^{14}			1.6×10^{12}	7.3×10^{13}	8.4×10^{11}	6.1×10^{12}	1.8×10^{12}	9.4×10^{11}

ALS parameters assume top-off mode operation at 500 mA stored current. Flux is in units of ph/s/0.1%BW and brightness is in units of ph/s/0.1%BW/mm^2/mrad^2.

The special considerations required for collecting infrared radiation produced by the bend magnets are discussed in detail in Section 5.4.

5.3 Parameters and Performance of Radiation Sources

The basic parameters characterizing the IDs, bending magnet, and three-pole wiggler sources are listed in Table 5.3.1. In the case of the NSLS-II bend magnet and TPW, the total power value is actually the power per horizontal mrad.

Table 5.3.1 Basic Parameters of NSLS-II Radiation Sources for Storage Ring Operation at 3.0 GeV and 500 mA

	U20	EPU45	DW90	SCW60	Bend Magnet	Three-pole wiggler
Type	IVU	EPU	PMW	SCW	Bend	PMW
Photon energy range [keV]	Hard x-ray (1.9–20)	Soft x-ray (0.180 – 7)	Broadband (<0.010 - 100)	Very hard x-ray (<0.010 – 200)	Soft and low-energy x-ray (<0.010 – 12)	Hard x-ray (<0.010 – 25)
Type of straight section	Low-β	Low-β	High-β	Low-β		
Period length, λ_U [mm]	20	45	90	60		
Total device length [m]	3.0	4.0	7.0	1.0		0.25
Number of periods	148	89	75	17		0.5
Minimum magnetic gap [mm]	5	10	12.5	15		28
Peak magnetic field strength in linear mode, B [T]	1.03	1.03	1.80	3.5	0.40	1.12
Max K_y*, linear mode	1.81	4.67	15.20	19.61		
Peak magnetic field strength in circular mode, B [T]		0.68				
Max $K_h = K_y$*, circular mode		2.87				
Minimum hν fundamental [keV]	1.62	0.183				
hν critical [keV]			10.8	21.0	2.39	6.7
Maximum total power [kW]	9.1	12.09	64.6	34.9		
Horizontal angular power density [kW/mrad]					0.023	0.064
On-axis power density [kW/mrad^2]	65.4	40.03	59.3	26.1	0.088	0.25

*K = 0.934 B[T] λ_u[cm]; effective K values listed

5.3.1 Brightness

For many experiments, especially those involving imaging or microscopy, where, for example, the beam must be focused down to a small spot, the key figure of merit of user radiation sources is their time average brightness. This is the flux output per unit bandwidth, per unit source area, and per unit solid angular divergence. Undulators and wigglers are excellent sources of high brightness radiation. The brightness of the baseline set of radiation sources for NSLS-II is shown in Figure 5.3.1. For the undulators, the tuning curves of harmonics 1, 3, 5, 7, and 9 are shown. These tuning curves show the variation of the peak brightness of the undulator harmonics as the magnetic field strength, and hence K parameter, is varied from K_{max}, listed for each undulator in Table 5.3.1, down to K_{min} ~0.4.

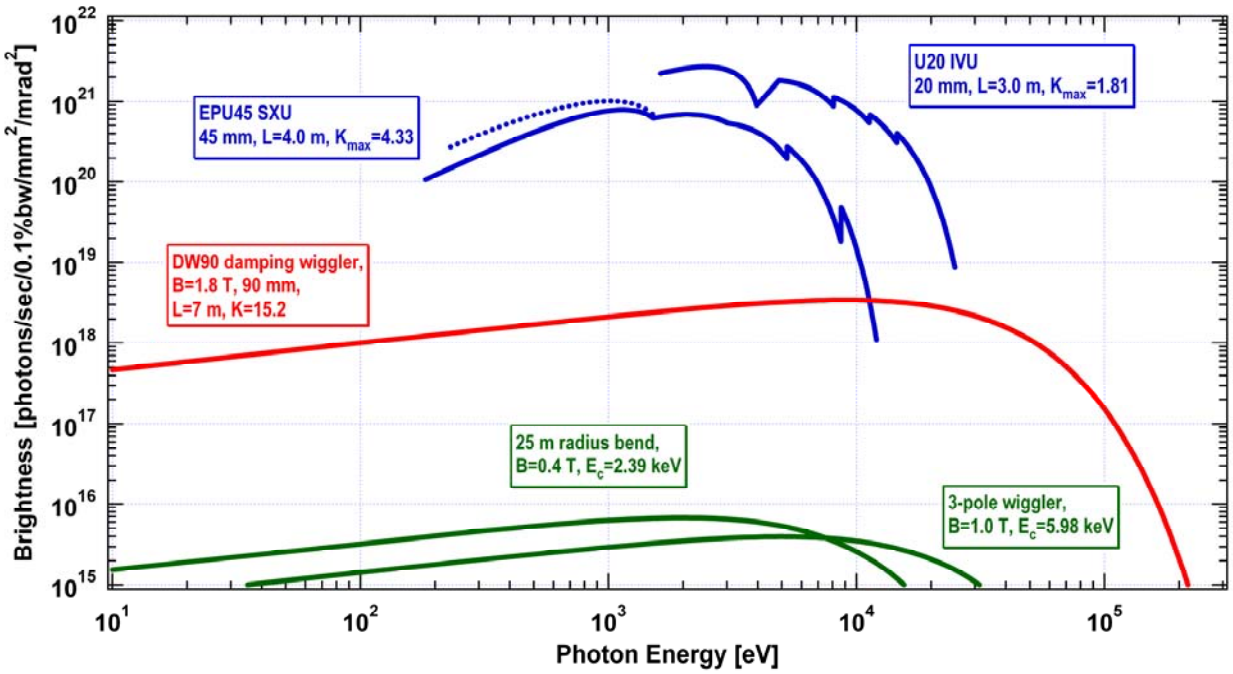

Figure 5.3.1 Brightness vs. photon energy for the baseline radiation sources at NSLS-II. Ring parameters: 3.0 GeV, 0.5 A, ε_h=0.5 nm, ε_v=0.008 nm, energy spread=0.001; Straight section parameters: low-β: β_h=2.02 m, β_v=1.06 m; high-β: β_h=20.8 m, β_v=2.94 m; $\alpha_h=\alpha_v=\eta_h=\eta_v=\eta'_h=\eta'_v=0$; Bend magnet parameters: β_h=2.62 m, β_v=20.3 m, α_h=1.75, α_v=-0.952, η_h=-0.129 m, η'_h=-0.102, $\eta_v=\eta'_v=0$; Three-pole wiggler parameters: β_h=3.87 m, β_v=35.2 m, α_h=2.01, α_v=-1.56, η_h=0.168 m, η'_h=-0.105, $\eta_v=\eta'_v=0$.

The brightness of the U20 hard x-ray undulator is the highest of any devices in the NSLS-II baseline configuration. This is due in part to the short period length of this device, thereby increasing the number of periods contributing to the flux output, and in part to the short output wavelengths compared to the soft x-ray undulator (EPU45). For diffraction-limited undulator radiation, which characterizes a good portion of the range of these two undulators, the brightness varies inversely as the square of the output wavelength. Note that the brightness of the U20 hard x-ray undulator exceeds the 10^{21} ph/s/0.1%BW/mm^2/mrad^2 level.

The wigglers provide broadband, high brightness sources of x-ray radiation. Each of the wigglers shown in Figure 5.3.1 covers nearly the entire photon energy range shown. The superconducting wiggler SCW60 is optimized for very high-energy x-ray work (i.e., above ~60 keV), while the damping wiggler DW90 is a high-flux, hard x-ray source with smooth spectral output extending down through the soft x-ray and VUV photon energy ranges.

Figure 5.3.1 shows the source brightness of the EPU45 soft x-ray undulator in two polarization modes: helical (or circular), shown as dotted lines, and linear, shown as solid lines. The circular polarized mode has intensity only in the fundamental and is slightly brighter than the linearly polarized mode at the same energy. It is expected that this mode will be used for all work below 2 keV, unless linearly polarized light is specifically required.

The NSLS-II bending magnet spectral brightness curve is also shown in Figure 5.3.1. The bending magnet spectrum is a bright source which extends from the infrared to the hard x-ray. This source will be useful up to a few times the critical energy of 2.39 keV, i.e., up to ~10 keV. The bending magnet brightness peaks at ~2 keV, making it an ideal broadband source in the soft x-ray (0.1–2 keV) and low-energy x-ray (2–5 keV) ranges.

The three-pole wiggler (TPW) source has a critical energy of 6 keV, making it a very useful continuum hard x-ray source up to ~25 keV. The TPW spectral brightness curve is shown in Figure 5.3.1. The emitted horizontal angular fan from these devices is 2 mrad wide.

5.3.2 Flux

For those experiments which do not require a very collimated and/or focused beam, the photon spectral flux is the key figure of merit. This is the number of photons per unit bandwidth per unit time, i.e. it is an angle-integrated quantity. For undulators, flux values typically quoted are integrated over the central angular cone, which contains essentially all of the usable flux from these devices. For wigglers and bend magnets, the flux value typically quoted is integrated over all angles vertically and over 1mrad horizontally. The horizontal angular dependence of bend magnets is uniform over its horizontal extent and, for wigglers, is maximum on axis and falls to zero at ±K/γ. For large-radius storage rings such as NSLS-II, the usable horizontal angular range will be determined by physical apertures in the beamline front end. The maximum horizontal angular range deliverable by NSLS-II insertion device front ends will be ~6mrad [check]. The corresponding value for bend magnets will be ~5mrad [check], whereas the three-pole wigglers will produce a 2mrad-wide horizontal angular fan. Figure 5.3.2 shows the flux for the NSLS-II radiation sources. The maximum flux is ~6×10^{15} ph/s/0.1%BW, reached by all three baseline insertion devices (DW90, IVU20, and EPU45) at the peaks of their output spectra (~0.2 keV, ~2 keV, and ~3 keV, respectively). As has been said previously, the bend magnets at NSLS-II will be superlative sources of high brightness and high flux radiation in the VUV and soft x-ray energy range. The three-pole wiggler sources are bend-magnet-like sources which extend into the hard x-ray energy range. Both the bend magnet and three-pole wiggler flux spectra peak at ~4×10^{13} ph/s/0.1%BW, per horizontal mrad.

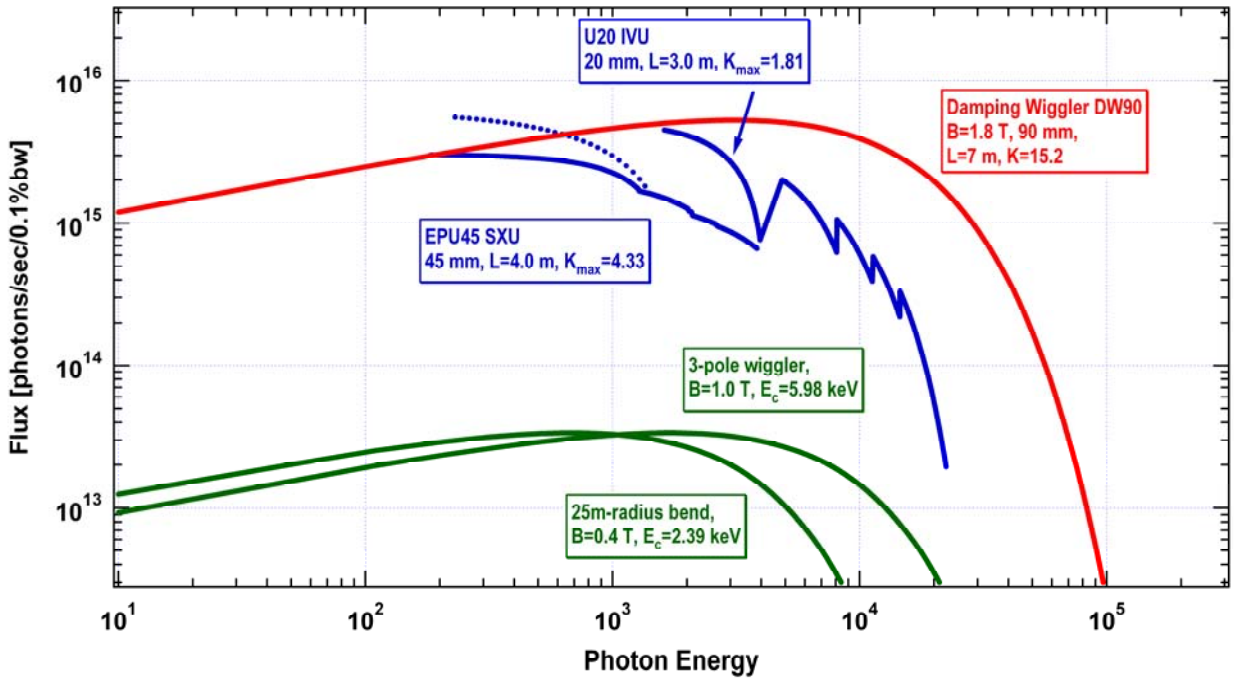

Figure 5.3.2 Flux output of baseline radiation sources at NSLS-II vs. photon energy. See the caption to Figure 5.3.1 for a listing of accelerator parameters used to calculate the flux curves shown here."

5.3.3 Power

Table 5.3.1 gives the maximum total output power of the NSLS-II radiation sources and Figure 5.3.3 shows how the total output power output of the undulators varies as their K value is changed from K_{min} (taken to be ~0.4) to K_{max}, as given in Table 5.3.1. For reference, the corresponding energy of the photons' radiation in the fundamental as a function of K is also given. The photon energy of harmonic n is n times that of the fundamental.

The total power radiated by the undulators at their maximum K settings (i.e., at minimum magnetic gap) is in the 8–13 kW range. The total power output from the NSLS-II wigglers is higher than that of the undulators, at nearly 65 kW, while that of the NSLS-II bend magnets and TPWs is very much less, at only ~23 W and 57W per horizontal mrad, respectively (see Table 5.3.1). Figure 5.3.3 also shows that the total output power at a given value of K increases by about a factor of two when operating in circular mode ($K_h = K_v \neq 0$) compared to linear mode ($K_h = 0$, $K_v \neq 0$) for the EPUs. The engineering challenges of handling the high heat loads in the insertion device front ends are detailed in Section [xx].

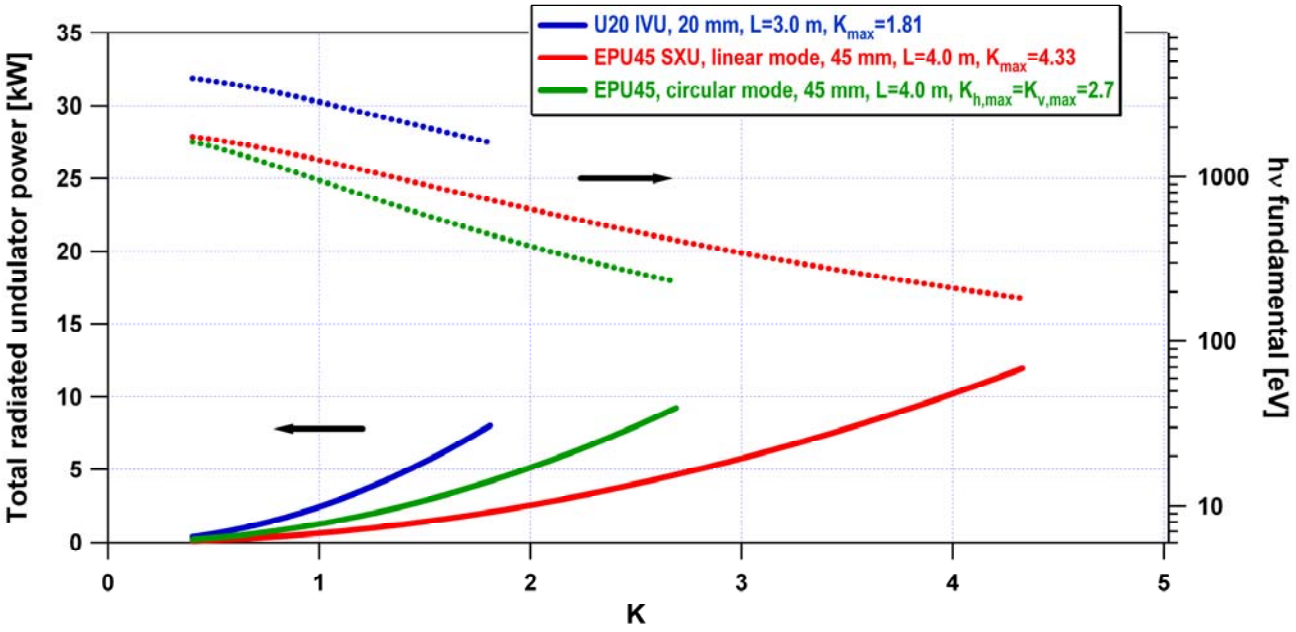

Figure 5.3.3 Total output power (left-hand axis) and fundamental output energy (right-hand axis) of the baseline NSLS-II undulators as a function of the undulator parameter, K.

5.3.4 Power Density

Table 5.3.1 gives the maximum (on-axis) angular power density of the NSLS-II radiation sources; Figure 5.3.4 shows how the maximum angular power density of the undulators varies as their K value changes from K_{min} (taken to be ~0.4) to K_{max}, as given in Table 5.3.1. For reference, the corresponding energy of the photons radiated in the fundamental as a function of K is also given. The energy of harmonic n is n times that of the fundamental. The maximum undulator angular power density radiated by the undulators at their maximum K settings (i.e., at minimum magnetic gap) varies from 40 to 65 kW/mrad^2. The wiggler angular power density output is in the 25–55 kW/mrad^2 range, while the bend magnet and TPW values are again very much less, at 88 W/mrad^2 and 220 W/mrad^2, respectively.

Figure 5.3.4 also shows that the EPU45 output angular power density in circular polarization mode is much lower than in linear polarization mode, and has a different dependence on K. This is primarily because in circular mode there are no higher harmonics, just the fundamental. An advantage of the circular

polarization mode is the lower output power density, which simplifies the design and operation of high energy-resolution beamlines by reducing the thermal deformations of the optical elements (see Chapter [xx]).

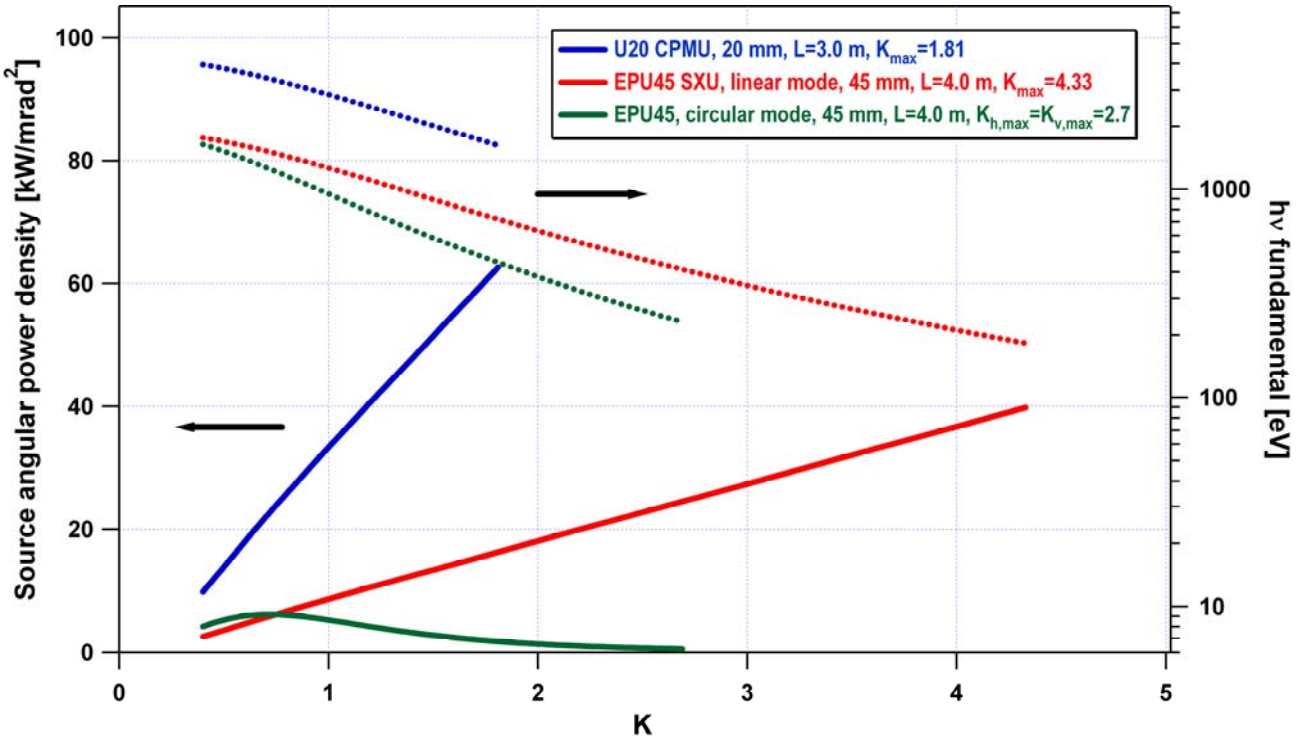

Figure 5.3.4 Angular power density (left-hand axis) and fundamental output energy (right-hand axis) of the baseline NSLS-II undulators as a function of the undulator parameter, K.

5.3.5 Photon Beam Size

The 1-σ effective photon beam size of the NSLS-II undulators is shown in Figure 5.3.5 as a function of photon energy. The lowest, straight (on a log-log graph) gray lines show the "natural" photon beam size, which is the size of a diffraction-limited photon beam for a zero emittance (and therefore zero size) electron beam. This diffraction-limited, "natural" photon beam size σ_{photon} is given by

$$\sigma_{photon} = \frac{1}{4\pi}\sqrt{2L\lambda} \quad . \tag{5.1-2}$$

One measure of the effective photon beam size, σ_{eff}, is given by the quadrature sum of the electron ($\sigma_{electron}$) and photon, σ_{photon}, contributions:

$$\sigma_{eff} = \sqrt{\sigma_{electron}^{\ 2} + \sigma_{photon}^{\ 2}} \quad . \tag{5.1-3}$$

The red and blue curves show σ_{eff} for the EPU45 SXU and U20 IVU undulators, respectively, in the vertical and horizontal planes, as labeled. Clearly, the undulator radiation is nearly diffraction-limited in the vertical plane over a wide photon energy range, from the far-infrared to ~2 keV. The deviation of the effective source size from the natural, diffraction-limited value is due to the contribution of the small, but finite, electron beam

size. The effective beam size in the horizontal plane is approximately an order of magnitude greater than the natural, diffraction-limited value at 10 keV, but at 10 eV and below is nearly diffraction-limited.

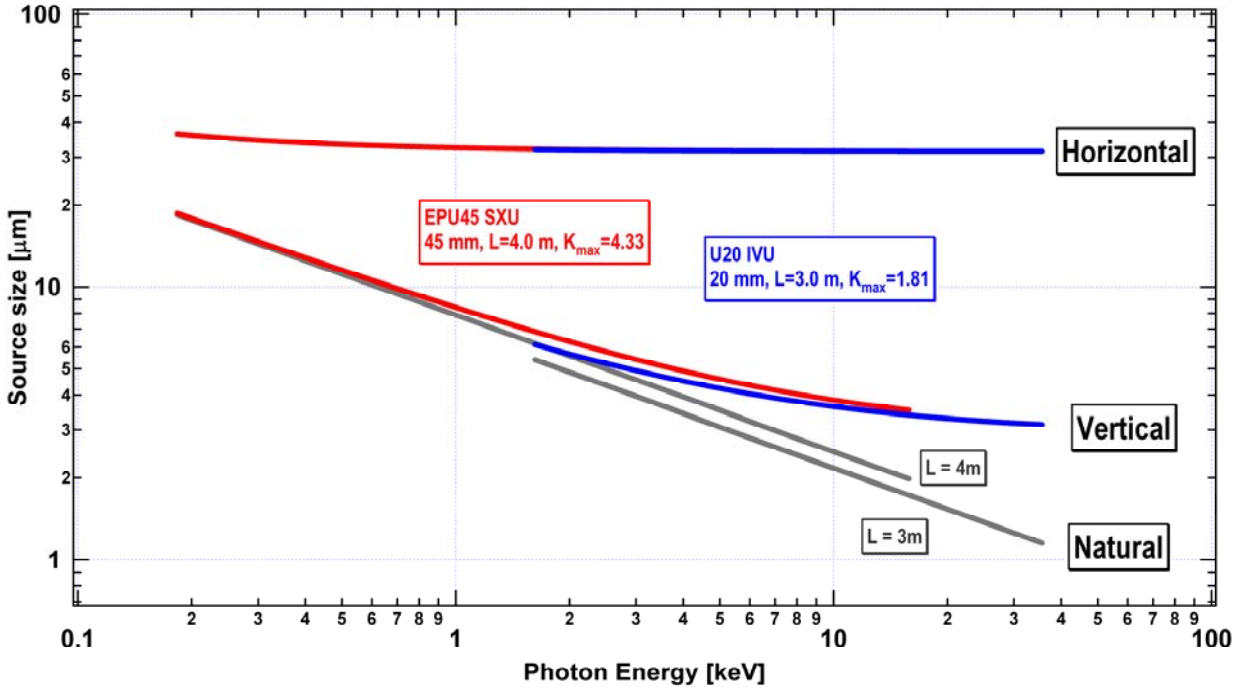

Figure 5.3.5 Photon beam source size in the horizontal and vertical directions for the NSLS-II undulators. The straight (gray) lines represent the corresponding diffraction-limited values (i.e., the zero electron beam emittance limit).

5.3.6 Photon Beam Angular Divergence

The 1-σ effective photon beam angular divergence of the NSLS-II undulators is shown in Figure 5.3.6 as a function of photon energy. The lowest, straight (on a log-log graph) gray lines show the "natural" photon beam angular divergence, which is the angular divergence of a diffraction-limited photon beam for a zero-emittance (and therefore zero angular divergence) electron beam. The diffraction-limited, "natural" photon beam angular divergence σ'_{photon} is given by

$$\sigma'_{photon} = \sqrt{\frac{\lambda}{2L}} \tag{5.1-4}$$

and the effective photon beam angular divergence σ'_{eff} is again given by the quadrature sum of the electron ($\sigma'_{electron}$) and photon (σ'_{photon}) contributions:

$$\sigma'_{eff} = \sqrt{\sigma'^{\,2}_{electron} + \sigma'^{\,2}_{photon}} \quad . \tag{5.1-5}$$

The red and blue curves in Figure 5.3.6 show σ'_{eff} for the EPU45 SXU and U20 IVU undulators, respectively, in the vertical and horizontal planes, as labeled. As in Figure 5.3.5 for beam size, Figure 5.3.6 shows that the angular divergence of the undulator radiation from NSLS-II undulators is nearly diffraction-limited in the vertical plane, and only somewhat less so in the horizontal plane, over the wide photon energy range from the far-infrared to ~2 keV. The deviation of the effective source angular divergence from the natural, diffraction-limited, value is due in part to the contribution of the tiny, but finite, beam angular divergence of the NSLS-II electron beam. In the horizontal plane, the effective beam angular divergence is

approximately a factor of 2 or 3 greater than the natural, diffraction-limited, value at 10 keV, but is nearly diffraction-limited at 10eV.

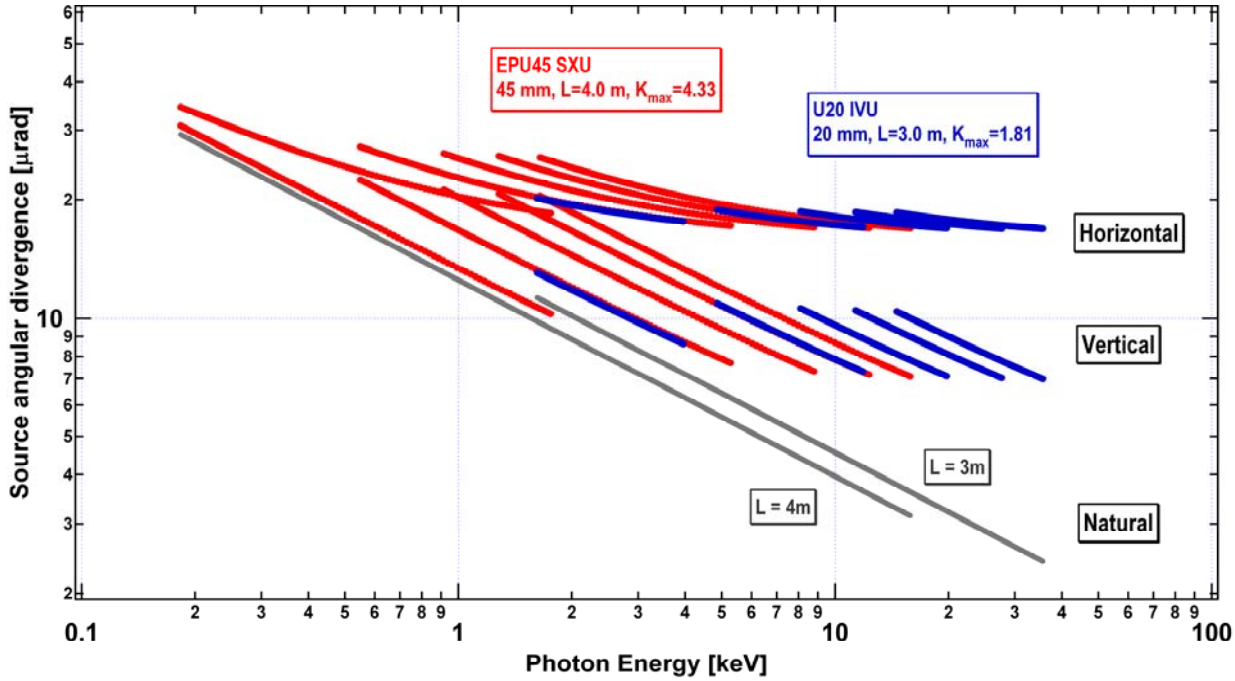

Figure 5.3.6 The angular divergence in the horizontal and vertical directions of the photon beam for the NSLS-II undulators. The straight (gray) lines represent the corresponding diffraction-limited values (i.e., the zero electron beam emittance limit).

The angular divergence is also limited by the finite energy spread of the electron beam. A noteworthy feature of Figure 5.3.6 is that the angular divergence of the various harmonics for a given undulator is approximately equal to that of the fundamental of that undulator. That is, it appears, empirically, that the angular divergence of undulator harmonic n is given by

$$\sigma_n' \approx \sqrt{\frac{\lambda_1}{2L}} \tag{5.1-6}$$

for n = 1, 3, 5, 7, or 9, in both the horizontal and vertical planes. This value is $\sqrt{\lambda_1}/\lambda_n = \sqrt{n}$ times larger than the zero-emittance angular divergence.

Thus, the limiting factor governing the vertical angular spread of the n>1 harmonics of NSLS-II undulators is the finite energy spread of the electron beam, which for the fully-damped case is $\delta E/E \sim 0.001$. This effect is stronger for the hard x-ray undulator (U20) than for the soft x-ray undulator (EPU45), but clearly affects both.

5.4 Infrared

The intrinsic infrared brightness of most synchrotron storage ring sources is determined entirely by the circulating beam current. This is certainly the case for the low emittance electron beam of the NSLS-II storage ring, and the goal of 500 mA beam current is very attractive from the standpoint of infrared performance. The ring is designed for an extremely stable beam; an important characteristic for the standard

rapid-scan interferometric techniques employed in most infrared spectroscopies. But designing an optical extraction configuration that preserves the brightness, while meeting mechanical and accelerator design constraints, can be quite difficult. Typically, the large angular collection needed to achieve an acceptable performance involves nonstandard construction geometries for the dipole chambers. These, in turn, can affect the beam impedance and lead to instabilities. A careful impedance analysis will be integral to the design of any dipole chamber intended for extracting infrared radiation, and efforts are underway to treat this issue quantitatively.

It is well known that dipole (bending) magnets produce infrared radiation by two distinct mechanisms: the conventional synchrotron radiation (bending magnet radiation) is produced in the body of the magnet, whereas edge radiation is produced as electrons enter or exit a dipole's magnetic field [5.4.1]. Infrared beamlines have been built to utilize one or the other of these source types, and sometimes both. For reasons outlined later in this section, we plan to meet most of the source requirements using bending magnet radiation, but also plan to collect and extract edge radiation. The beamline design and performance analysis described in Chapter 11 will take both source types into account.

5.4.1 Bending Magnet Source

The collection efficiency for conventional dipole bend radiation is determined by the natural opening angle for synchrotron radiation in the long wavelength limit. For a wavelength λ and bend radius ρ, the RMS half-angle is defined as:

$$\theta_\lambda = \left(\frac{3}{4\pi} \frac{\lambda}{\rho} \right)^{1/3} . \qquad (5.4\text{-}1)$$

From this expression we see that the large bending radius (ρ ~25 m) of NSLS-II dipoles causes the infrared to be emitted into angles 2.35 times smaller than for the existing NSLS VUV/IR ring (ρ ~1.9 m). Thus, the performance for NSLS-II with 38 mrad extraction would be identical to a 90 mrad extraction from the VUV/IR ring. A study of the NSLS-II dipole design indicates that a horizontal extraction of 50 mrad is achievable (plus an additional 5 mrad on the "negative side", useful for collecting edge radiation). This is based on an infrared extraction where the second dipole in a DBA cell is used in order to stay clear of any potential insertion device beamline (Figure 5.4.1). The large bending radius makes extraction increasingly difficult as one continues toward the second half of a dipole, giving rise to the 50 mrad horizontal collection limit.

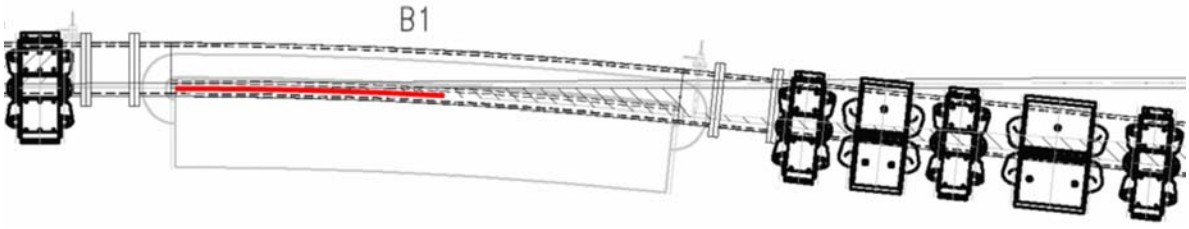

Figure 5.4.1 Drawing of the second dipole magnet in the NSLS-II DBA 30 lattice. Red line indicates the candidate IR source orbit segment. Approximately 50 mrad of horizontal collection appears feasible, including the zero degree segment for edge radiation.

The standard NSLS-II dipole bending magnets allow a vertical chamber dimension of ~25 mm and represent another constraint for infrared, limiting the vertical collection to approximately 16 mrad (the value varies from 12 mrad up to 20 mrad due to the large source depth). While this is adequate for mid-infrared spectroscopy as used in chemical imaging, it limits the performance for far-infrared spectroscopy due to the relatively large angles into which this radiation is emitted. Therefore, we are planning for a second dipole

magnet design for use on far-infrared ports. This dipole would have a ~60 mm (or larger) gap and would accept a dipole chamber providing an average 32 mrad of vertical collection (and potentially up to 48 mrad with a larger dipole gap). The need for such a large aperture port becomes even more apparent when one considers the shielding effects of a conducting dipole vacuum chamber. The subject has been treated most thoroughly by Bosch [5.4.2] who confirmed (theoretically) that bending magnet radiation is suppressed for wavelengths greater than an effective cutoff value given by $\lambda_c=(h^3/\rho)^{1/2}$ where h is the chamber height and ρ is the bending radius. The large bending radius of NSLS-II, combined with a standard chamber height of 25 mm, results in a cutoff wavelength of 800 μm, effectively removing the portion of the THz spectral range most important for magnetospectroscopy. This provides another compelling reason for a larger dipole chamber and 60 mm gap dipole magnet. Indeed, increasing the dipole gap an additional 30 mm (to accept a 75 mm vertical height chamber) would shift the cutoff wavelength to beyond 4 mm. In all cases, the detailed dipole chamber design and transitions will require careful study in terms of electron beam impedance and potential instabilities. Our initial impedance analysis for a 50 mm high chamber appears promising and suggests that an even larger (75 mm) chamber would be feasible. However, more detailed calculations will be needed for actual chamber mechanical designs to ensure no instability problems will arise.

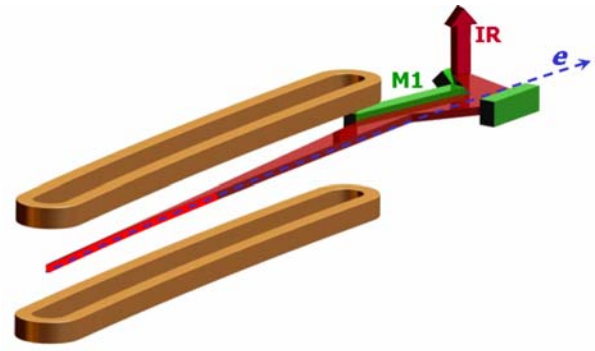

Figure 5.4.2 NSLS-II Infrared Dipole Radiation Extraction. The bright red segment marks the electron beam segment serving as an infrared source. The radiation is collected by a long mirror (M1) and reflected out of the dipole chamber by a second and third mirror combination.

The extraction arrangement for NSLS-II is proposed to have the 1st mirror optic integrated into the dipole chamber construction. The metal mirror can be made to be electrically contiguous with the chamber wall to minimize impedance effects. The oblique angle of incidence and soft x-ray spectrum from the large NSLS-II dipole bending radius limits the local power load on this optic to well under 1 kW/cm^2, such that a special slot or cooling mask may not be required (Figure 5.4.2). Finite element analysis will be performed on candidate mirror materials (e.g., aluminum or copper) to confirm that this heat load can be directly managed without significant optical distortion of the surface. Initial studies of the required optical figure for this 1st mirror suggest that a simple toroidal shape will suffice, allowing conventional diamond turning to be used in its construction (Figure 5.4.3). The remaining optical elements can be either conventional aluminized glass or diamond-turned aluminum to meet specific optical design requirements.

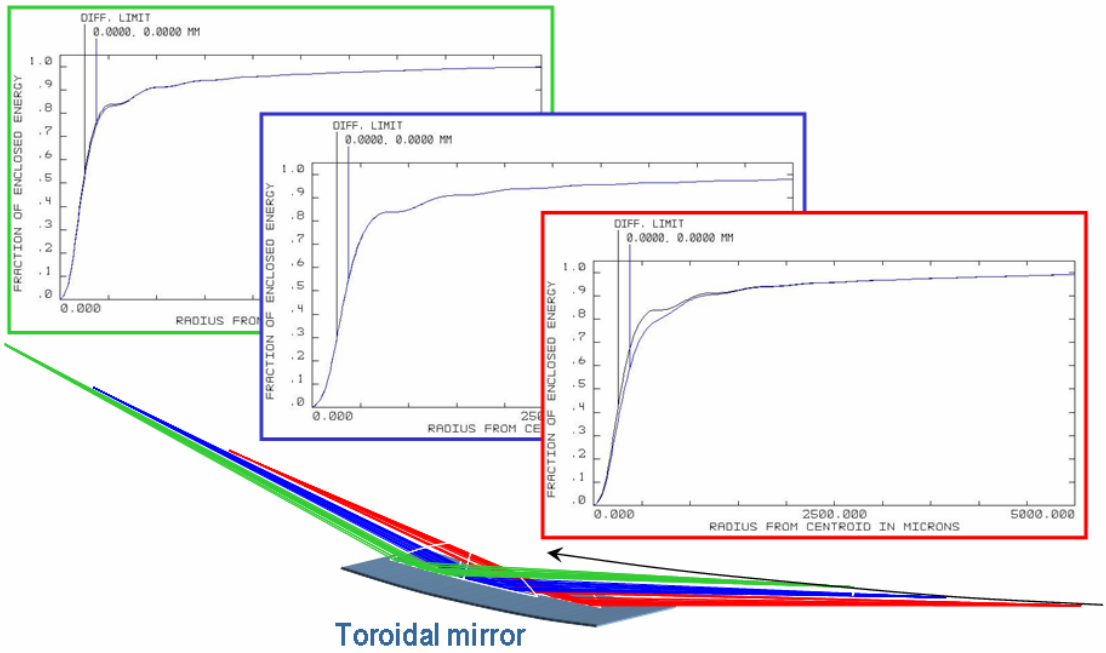

Figure 5.4.3 Extraction Optical Performance. ZEMAX optical analysis for a toroidal first mirror optic when used to focus a dipole bend/arc source at a wavelength of 6 μm (mid-infrared). Near diffraction limited performance is achieved along the entire source length.

A detailed performance comparison for these NSLS-II dipoles and the existing VUV/IR ring dipoles can be made using the standard expressions for dipole synchrotron radiation in the low frequency limit. The flux calculations can be compared to results from other synchrotron radiation source codes such as SPECTRA [5.4.3] or SRW [5.4.4] to check for consistency. Though some of these calculations are for the photon flux, they can be used for comparing brightness whenever the source's physical dimensions are smaller than the diffraction limit (the case for all IR wavelengths on NSLS-II, and IR wavelengths longer than 10 microns for the existing NSLS VUV/IR ring). We find that all three calculations agree to within 10% for the intrinsic flux of dipole radiation when multiparticle coherence and chamber shielding effects are ignored. Note that one can convert from units of ph/s/0.1%BW to watts per wavenumber, multiplying by 2×10^{-20}. Calculation results are shown in the Figures 5.4.4 and 5.4.5, along with a calculation for an existing port on the VUV/IR ring, indicating that NSLS-II can serve as a highly competitive, and indeed, world-leading, storage ring source for infrared.

Details of these calculation results show that an extraction based on a conventional NSLS-II dipole (average of 16 mrad vertical and 50 mrad horizontal) will be sufficient for mid-infrared spectroscopy, including microprobes and imaging. We envision two options for such mid-infrared extractions. In one option, the beam is divided horizontally to simultaneously serve two or three mid-infrared microprobe end stations. The three collections (in order of entering the dipole) would be (H×V) 15×12 mrad, 15×16 mrad, and 20×20 mrad. The varying vertical aperture is due to the changing distance between the first collecting mirror and the collected source segment as a function of horizontal position (angle). The performance for any of these extractions exceeds the present performance of the NSLS VUV/IR ring over most of the mid-infrared. Only at the long wavelength (low frequency) end of this spectral range are the three extractions distinguishable, with the 20×20 mrad outperforming the other two. But it should be noted that the initial 15×12 mrad collection also includes the zero-degree component, giving this the added feature of edge radiation (not included in the brightness calculation). In the other option, the entire horizontal swath is fed into a single microspectrometer end station based on a focal plane array detector for large area imaging, as

described in Chapter 11. The detailed optical system for matching the source to the instrument will be the subject of further research.

In the far-infrared, the brightness for a conventional dipole (16 mrad average vertical extraction) continues to fall away from the ideal value and below the present performance for the NSLS VUV/IR by a factor of 5 at 25 cm^{-1} (400 μm wavelength). The degradation below 10 cm^{-1} becomes even more severe when the shielding effect of the 25 mm high dipole chamber is taken into account. Note that the shielding effect for dipole radiation is a complex subject, and we have taken it into account using a simplified approach. In this approach, it is assumed that radiation unable to couple into a propagating waveguide mode of the chamber is completely lost, and is roughly equivalent to truncating the effective near-field source size to a dimension equal to the chamber height (see [5.4.2], condition 2 for strong shielding). A large-gap dipole enables greater vertical collection efficiency and also shifts the shielding cutoff to lower frequencies. This is illustrated in the brightness calculations of Figure 5.4.5, which includes curves for the standard NSLS-II dipole extraction (50×16 mrad) plus two candidate large-gap dipole extractions (50×32 mrad based on a 50 mm high dipole chamber, and 50×48 mrad based on a 75 mm high dipole chamber). Also shown is the existing performance for the NSLS VUV/IR ring's 90×90 mrad ports plus the very large port beamline at the UVSOR facility (Okazaki, Japan) that represents the most competitive far-infrared beamline elsewhere in the world. (Note: This does not take into account the coherent THz synchrotron radiation mode of operation developed at BESSY and proposed for CIRCE by the ALS/Lawrence Berkeley Lab.) The 50×48 mrad configuration would maintain the NSLS lead in the area of incoherent THz synchrotron radiation, and provide excellent ports for studying aspects of coherent synchrotron radiation production, a subject of great interest for future source development. Any of these ports would offer excellent mid-infrared performance.

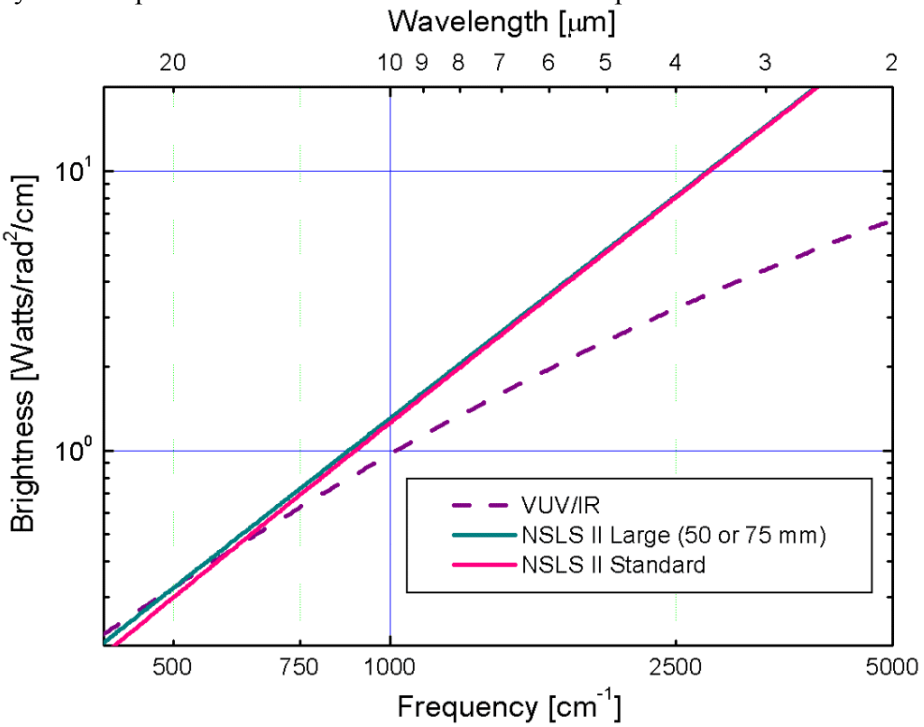

Figure 5.4.4 Calculated NSLS-II brightness for the mid-infrared spectral range, comparing the existing VUV/IR ring with the two proposed for NSLS-II extractions. Note that the lower emittance of NSLS-II leads to brightness improvements over much of this spectral range and that the standard dipole chamber height of 25 mm is sufficient for this spectral range.

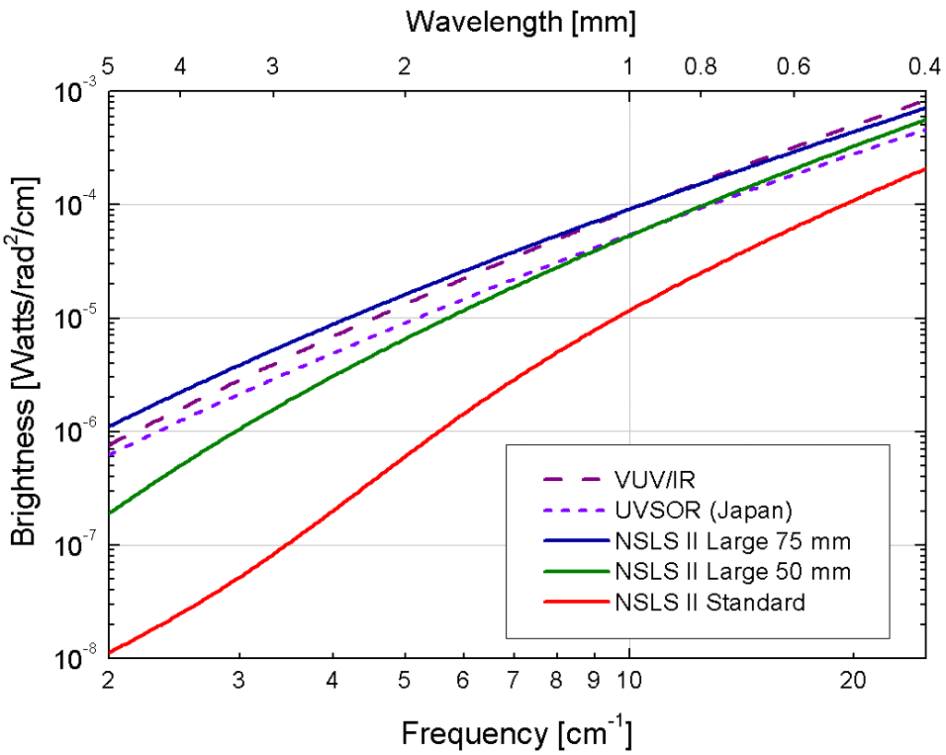

Figure 5.4.5 Calculated NSLS-II brightness for the very far-infrared spectral range, comparing the existing VUV/IR ring with three collection geometries for NSLS-II having vertical dipole chamber heights as shown, plus a high-performance beamline at UVSOR. The cutoff effect of the standard-gap dipole chamber and 16 mrad collection can be clearly seen for wavelengths greater than 1 mm.

5.4.2 Dipole Edge Source

The proposed infrared extraction geometry allows for collection of the zero-degree segment from the dipole (in line with the upstream straight section), including ~5 mrad on the opposite side. This will allow for the extraction of dipole edge radiation [5.4.1]. Dipole edge radiation has characteristics similar to transition or diffraction radiation, e.g., radial polarization. In contrast to bending magnet radiation, the far-field angular distribution for edge radiation is contained mostly within a cone of angle $\theta = 1/\gamma$. This implies an effective source size of $\lambda\gamma$ and a very long formation length of $\lambda\gamma^2$ such that computations designed exclusively for the far-field are no longer accurate. An added complication stems from the fact that dipole edges typically occur in pairs, leading to a ring-like interference pattern that depends on wavelength. The SRW code [5.4.4] includes near-field terms suitable for calculating edge radiation in the ideal case where the ring chamber has no shielding effect on the radiation. An example result from SRW is shown in Figure 5.4.6, and illustrates both edge radiation (ring-like pattern at right) and bend radiation (broad smear extending to left). The actual projection of the beam onto the first mirror optic will be stretched horizontally about a factor of 3 compared to these views (due to the 75° angle of incidence for the radiation).

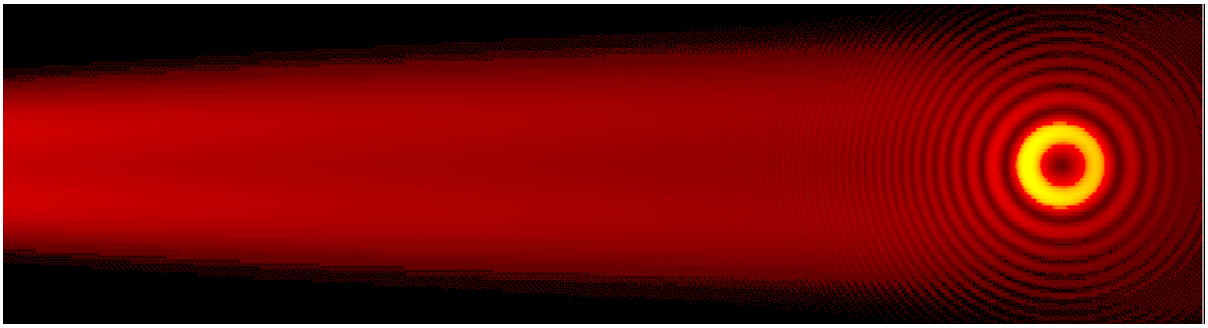

Figure 5.4.6 SRW analysis for 55 mrad (-5 to +50) horizontal and 12 to 20 mrad vertical collection of 6 μm wavelength infrared radiation produced in the leading section of an NSLS-II dipole bending magnet. The ring pattern is due to interference from the back edge of the previous dipole, located 5.6 meters upstream (distance between dipole edges in a DBA cell). The broad stripe of radiation extending to the left is the conventional bending magnet radiation.

Though a few infrared beamlines based on edge radiation exist (e.g., at ANKA/Karlsruhe, SRC/ Wisconsin, and ESRF/Grenoble), the detailed performance at long wavelengths has not been formally demonstrated. There are two reasons to be concerned about the long wavelength performance. First, the radius of the first constructive interference ring moves outward with increasing wavelength such that the collection through a finite aperture will suffer. Second, the large effective source size is expected to cause a shielding (waveguide) cutoff when the wavelength exceeds h^2/R, where h is the chamber height and R is the distance from the source to the collecting aperture [5.4.2]. Our extraction aperture would be situated approximately 3 meters away from the source point and, with a nominal chamber height of 25 mm, the cutoff would begin at a wavelength of ~200 μm such that a significant portion of the very far-infrared would be lost. Edge radiation also introduces complications for mid-infrared microspectroscopy and imaging due to its radial polarization. The source itself is point-like, making it less suitable for illuminating large area focal plane array detectors that are expected to become the standard approach for delivering large area, high-resolution images. For these reasons, our infrared extraction will be based primarily on conventional bending magnet radiation, but we will have the opportunity to exploit the unique characteristics of edge radiation where beneficial.

References

[5.4.1] R.A. Bosch et al., *Rev. Sci. Instr.* **67,** 3346 (1996); Proceedings of the Ninth Nat'l Conf. on Synch. Rad. Instrum., Argonne, IL, (1995.)
[5.4.2] R.A. Bosch, *Nucl. Instrum. & Meth. Phys. Res.* A **482**, 789 (2002).
[5.4.3] T. Tanaka and H. Kitamura, *J. Synch. Rad.* **8**, 1221 (2001)
[5.4.4] O. Chubar and P. Elleaume, *Proc. of the EPAC98 Conference*, 1177 (1998).
[5.4.5] G.L. Carr, *Vibrational Spectroscopy* **19**, 53 (1999); R.P.S.M. Lobo, et al., *Rev. Sci. Instrum.* **73**, 1 (2002).

5.5 Conceptual Magnetic Designs for the IDs

In Section 5.1 we specified the types of insertion devices that are needed to meet user requirements and to achieve the unprecedented brightness goals of NSLS-II. We presented the optical performance and spectral characteristics of these IDs. They are based on proven designs, and in some cases push the state of the art in what we believe to be rational and realizable extensions of existing technology. In this section we present conceptual magnetic designs of the various ID types that will meet the performance requirements and constraints. We also identify and describe the R&D and prototyping needed to verify each design concept, to resolve any unknowns, and to test advanced concepts for future upgrade paths. We describe novel mechanical concepts that may simplify ID designs and/or improve their performance. Finally, we describe magnetic measurement systems that will be developed to verify and optimize ID performance.

Section 5.5.1 deals with the damping wiggler, which is also used as a broadband source.

Section 5.5.5 discusses tunable, planar, hard x-ray sources, specifically the mini-gap, in-vacuum undulator (IVU) as a baseline device, and its most recent evolution, the cryo-permanent magnet undulator (CPMU).

Section 5.5.3 describes variable polarization devices for soft x-rays and vacuum ultra-violet. The baseline design is an Apple-II type machine. An alternative HiSOR-type design was considered.

Section 5.5.4 addresses using a permanent magnet three-pole wiggler (3PW) to meet the needs of the current users of hard X-ray bending magnets at NSLS.

In Section 5.6, the IDs to be installed or considered in later stages of beamline construction will be discussed. Those devices are the superconducting wigglers (both low- and high-temperature types), superconducting undulator, quasi-periodic undulator, and revolver-type undulator. Also discussed in Section 5.6 is the development of an insertion device Magnetic Measurement Facility (MMF).

5.5.1 Damping Wigglers

Earlier we defined two key parameters of the damping wigglers (DWs): the operating peak field of 1.8 T and an eventual total length of 56 m. The peak field value was chosen to be high enough to radiate sufficient power for adequate emittance damping, but not so high as to create excessive energy spread. The DWs are also useful as high-flux, high-brightness broadband sources in the hard x-ray range.

The initial installed length of DWs will be 21 m, composed of six wigglers, each 3.5 m long. A third key design parameter is the minimum magnetic gap. The estimated vertical stay-clear aperture at ±3.5 m from the center of long straight section is 9.5 mm. Allowing for beamtube wall thickness of 1 mm, plus 0.5 mm clearance between the beamtube and the magnet poles, we obtain a minimum magnetic gap of 12.5 mm. From empirical design formulas developed by Elleaume for various planar undulator (wiggler) technologies [5.7.15], we find that 1.8 T peak field can be produced at that gap by a conventional PM-hybrid wiggler with a period of 90 mm, using high-field NdFeB magnets (Br = 1.2 T) and vanadium permendur poles. However, the total radiated power from such a wiggler is less than that by the device with ideal sinusoidal field due to longitudinal higher harmonics contents. Therefore, special care is needed to optimize the field profile. Unlike users of undulator radiation, wiggler users expect a broad, dipole-like spectrum. Therefore, minimizing phase errors is not important. Shimming of DWs is concerned mainly with trajectory straightness and multipoles. In fact, gap taper, or variation in pole periodicity are sometimes introduced in wigglers intentionally to spoil coherence and to smooth the spectrum.

DWs must meet the same integrated dipole and multipole error specifications imposed on all IDs. However, since they will operate at fixed gap, these errors can be shimmed out more easily than in variable-

gap IDs, without concern about gap-dependence. The next sections discuss some additional design considerations for DWs.

5.5.1.1 Dynamic Field Integral

The integrated field seen by sinusoidally wiggling electrons [5.5.1.1] is

$$\int B_y ds \approx \frac{-L}{2k^2 B\rho} B_y(x_i) \frac{dB_y(x_i)}{dx}, \quad (5.5.1\text{-}1)$$

where L is the device length, k_w is the 2ρ/period length, ρ is the radius of curvature of the trajectory, and x_i is the horizontal displacement of the electron. This is called dynamic field integral, and it scales as ID period squared and as the derivative of the transverse field roll-off. An important aspect of optimization of long-period wiggler magnetics is how to determine the necessary transverse pole width to minimize the effect of the dynamic field integral effect while minimizing attractive force, which is proportional to the magnet area, and keeping the cost as low as possible. Beam tracking reveals the detrimental effect of this integral on the beam dynamics. However, ordinary magnetic measurement method in straight line is incapable of measuring this effect. Therefore, careful modeling effort is required for long period device.

5.5.1.2 Attractive Force and Size/Cost Challenges of the Damping Wigglers

For NSLS-II, the damping wigglers will be used as a broadband source. The design calls for 7 m of damping wiggler in an 8 m straight. In reality, it is easier to combine two 3.5 m devices. The approximate attractive force of a planar device is given as follows:

$$F_{ID} \approx \frac{B_y^2 WL}{4\mu_0}, \quad (5.5.1\text{-}2)$$

where W is the horizontal width of poles or magnets, L is the total length of the device, and μ_0 is the permeability of the vacuum. With W = 80 mm and B_{oy} = 1.8 T, the attractive force per meter is about 60 kN. A variable-gap device must have a structure that is rigid enough not to create intolerable multipole components due to defection. As this is an out-of-vacuum device, many different designs have worked properly in storage rings.

Wigglers of this type, from 2 to 4 meters in length, have been designed and build to specification by industry for many synchrotron light sources. The mechanical structures to support and control the gap of these wigglers are generally massive and expensive for variable gap device. However, NSLS-II DW is designed to operate at a fixed gap, no strict parallelness of magnet arrays is required at other gap positions. On the other hand, the available cross section of a device for NSLS-II is substantially smaller than other equivalent facility due to the lower beam height (1.0 m compared to 1.2-1.4 m for most of facilities in the world) and due to the need to have extra space in the tunnel for emergency evacuation. A detailed design study will consider alternative magnet configurations that could lessen the need for these massive structures while maintaining the structural rigidity. The goal of this project is to design a magnet configuration that can utilize a relatively compact, lower-cost magnet support system that ultimately could reduce the cost of these wigglers significantly.

5.5.1.3 Non-Sinusoidal Field Effect

Another issue for long-period undulators is the deviation from sinusoidal field, which effectively reduces the deflection parameter. (This is not an issue for wigglers, where the critical energy depends on peak field only.) We examine a hybrid undulator with side magnets and permendur poles with the parameters shown in Table 5.5.1.1.

Table 5.5.1.1 U90 Wiggler Parameters.

Period length [mm]	90
Nominal peak field [T]	1.8
Remanent field (B_r) [T]	1.20
Gap [mm]	12.5
Magnet horizontal size [mm]	140
Magnet vertical size [mm]	95
Main Pole horizontal size [mm]	80
Main Pole vertical size [mm]	75
Air gap [mm]	0.1
Chamfer (magnet) [mm]	2.0
Chamfer (pole) [mm]	1.5
Corner cut (magnet) [mm]	3.0
Gap offset (magnet) [mm]	0.25

By varying the pole thickness while keeping fixed the total period length, we have calculated the peak magnetic field (induction) and effective K_y, as shown in Table 5.5.1.2. When the pole thickness is reduced from 21 to 19 mm, the peak field increases from 1.80 to 1.85 T and effective K_y decreases from 15.2 to 15.1. This indicates that the field deviates too much from the sinusoidal form.

Table 5.5.1.2 Comparison of Peak K_y and Effective K_y with Varying Pole Width (Period Length=90 mm)

Pole Thickness (mm)	Peak Field (T)	Peak Ky	Effective Ky
19	1.85	15.6	15.1
20	1.83	15.4	15.2
21	1.80	15.2	15.2
22	1.75	14.7	15.1

The effective K value should be close to the peak K value of a sinusoidal wave of peak amplitude of 1.8T to obtain equal amount of radiated power assumed in emittance reduction calculation. The following quantity was numerically calculated over one period to compare the value with sinusoidal field.

$$P_{per} = \int_{L}^{-L} B_y^2 ds \qquad (5.5.1\text{-}3)$$

where L=period length /2. With pole thickness of 21 mm, the effective field appears to be closest to that of ideal sinusoidal field. $P_{per} = 1.01\ P_{per}$ (ideal).

5.5.1.4 Baseline Damping Wiggler Design

A hybrid structure with side magnets and permendur poles has been chosen for the NSLS-II device. Soft iron poles are significantly cheaper than permendur but produce slightly lower field. Figure 5.5.1.1 is an isometric rendering of the W90 magnet arrays by Radia. The side magnets shown in magenta have identical size; two different sized magnets are shown in green. Pieces in yellow represent permendur poles. Figure 5.5.1.2 shows the end view of the array.

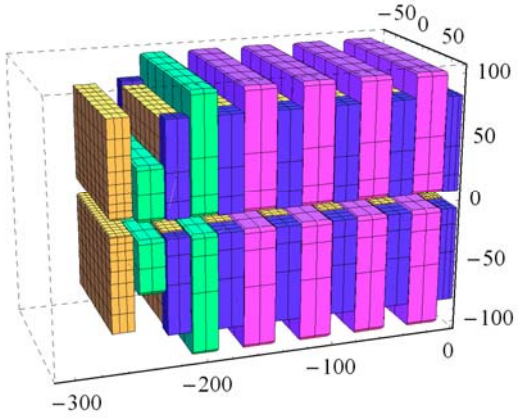

Figure 5.5.1.1 Magnet arrays of W90. Only the first few periods are shown, for clarity. Units are millimeters.

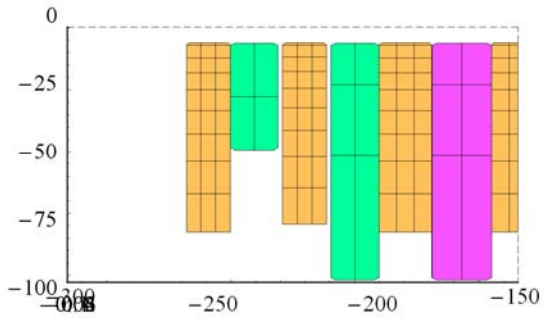

Figure 5.5.1.2 End view of W90.

The field and trajectory computed from the model are plotted in Figure 5.5.1.3, for a gap of 12.5 mm. The trajectory is calculated by a particle-tracking Runge-Kutta routine. The particle is launched with zero offset and angle (x = 0, x' = 0), and its position and angle are calculated every 2.5 mm (36 points per period). The amount of change in the first integral can be easily compensated by external coils.

a

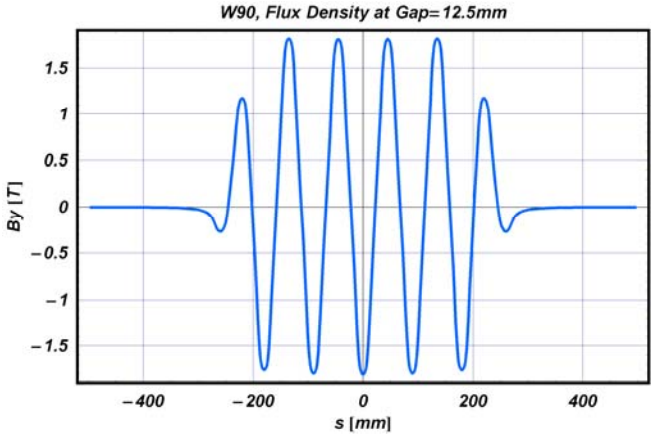

Figure 5.5.1.3 Field, angle, and trajectory plots for the five-period model of W90.

a) Vertical magnetic flux density at a gap of 12.5 mm.

b

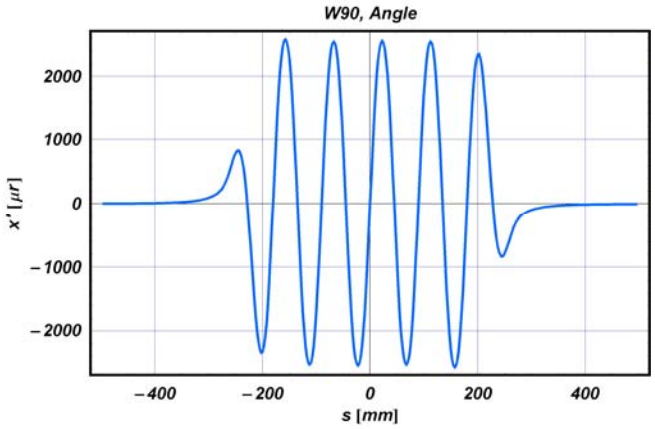

b) Horizontal angle at a gap of 12.5 mm.

c

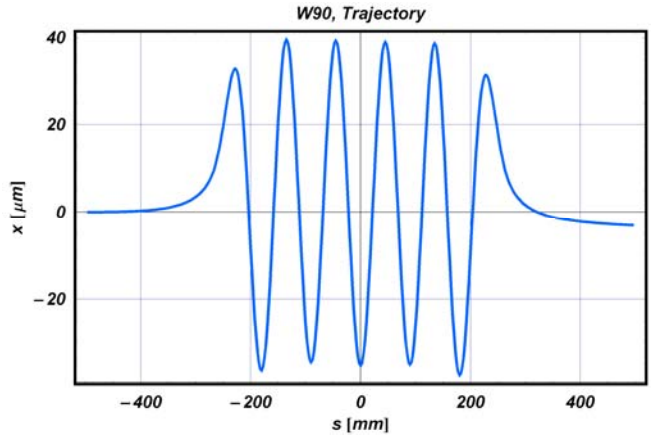

c) Horizontal trajectory at a gap of 12.5 mm.

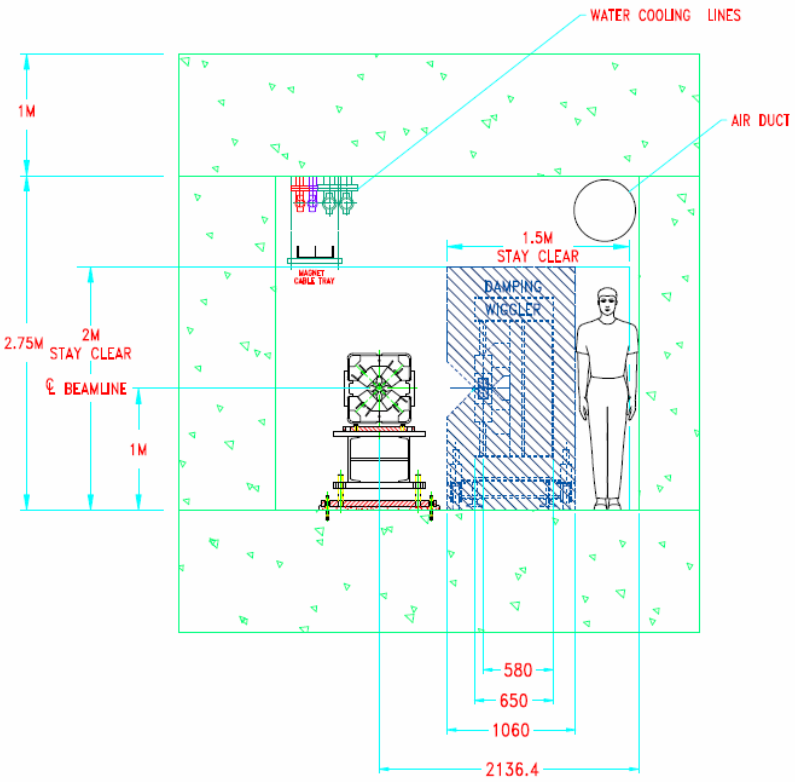

Figure 5.5.1.4 Available cross section of NSLS-II DW.

There is one challenging requirement for all NSLS-II insertion devices. That is an unusually restricted transverse cross section available for the devices. Firstly, the NSLS-II beam height is only 1.0 m compared to 1.4 m at many U.S. facilities and 1.2 m at some European and Japanese facilities. Secondly, the horizontal size is limited due to safety requirement which demand certain space in the tunnel during device transport. The external dimensions of the NSLS-II DW must conform to the envelope shown in Figure 5.5.1.4. Preliminary FEA analysis with 63 kN/m attractive force was carried out by STI Optronics, Inc. The result is shown in Figure 5.5.1.5, where the units for transition are shown in inches. These deformation translates approximately 3.9 mrad of roll angle for each strongback, which can be compensated for operating gap.

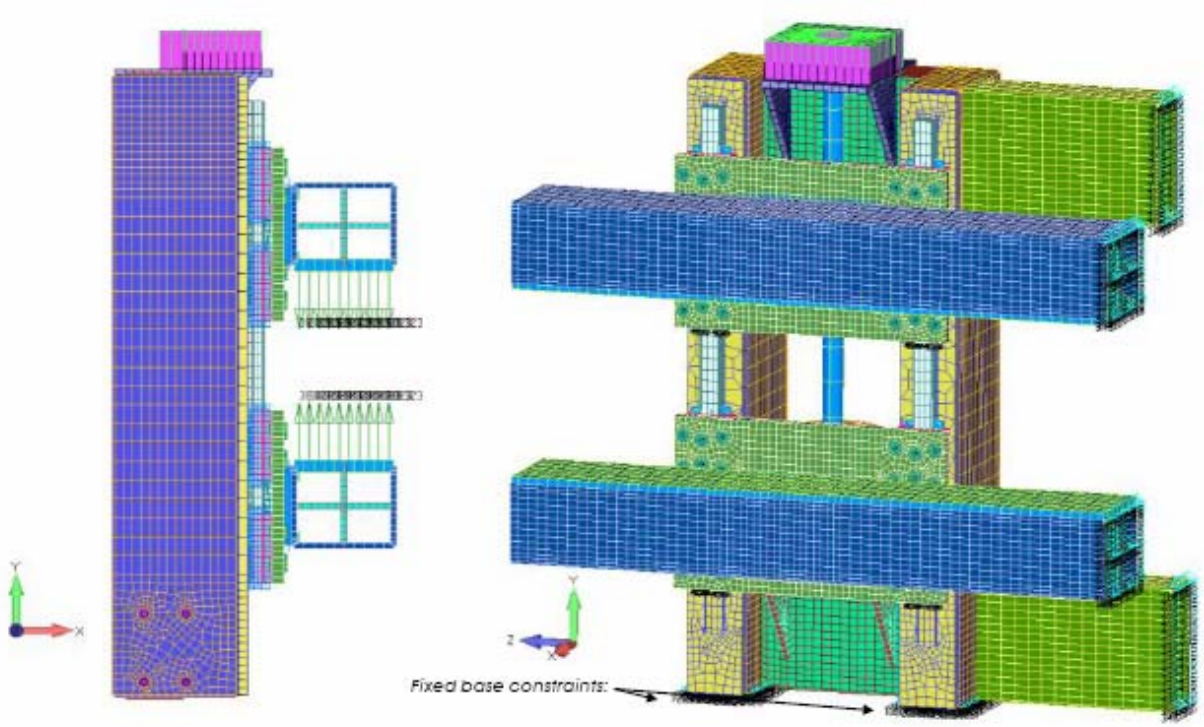

Figure 5.5.1.5 FEA analysis model

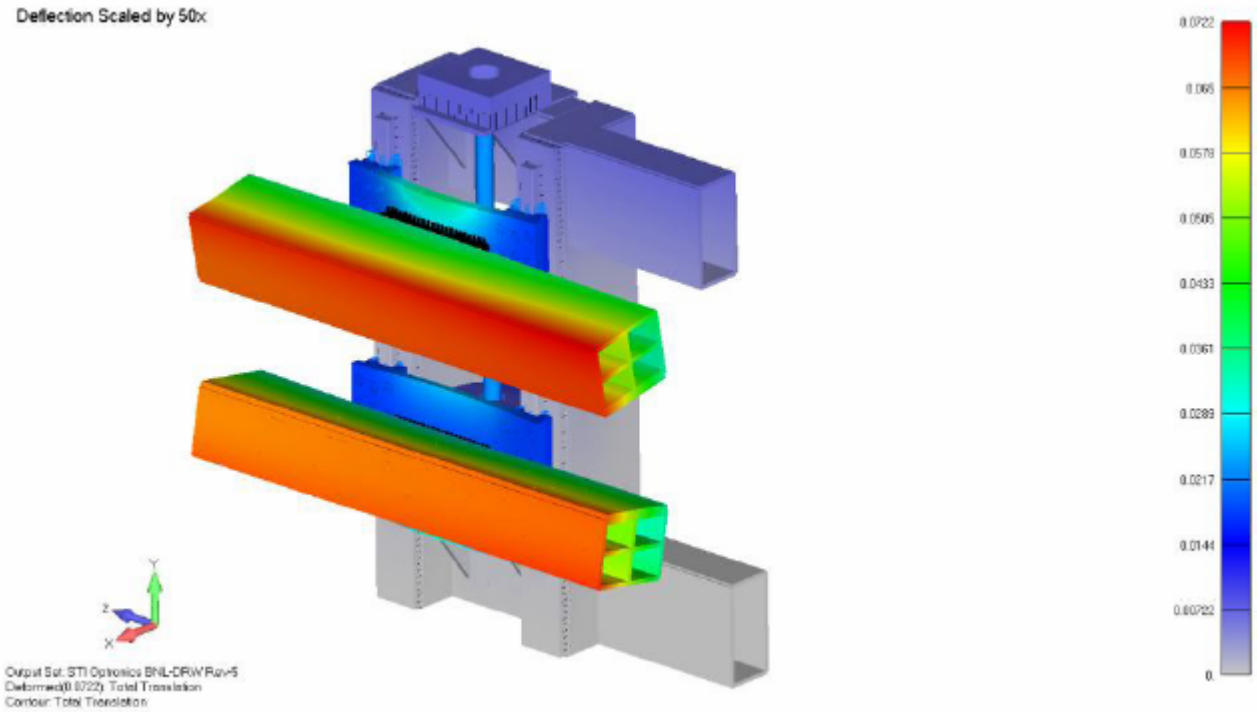

Figure 5.5.1.6 Displacement plot

5.5.1.5 R&D Elements for DW Development

Superconducting devices, especially HTS versions, can be considered as an alternative choice for DWs. However, unlike user devices, these DWs are an integral part of the light source lattice and any failure would result in the degradation of emittance, which affects all the users in the facility. Therefore, it is essential to achieve extremely high reliability for the SCWs to be considered as an alternative for PM-based DWs. Extensive reliability studies will be necessary if this option is pursued.

Another subject is a novel gap separation mechanism, which should simplify the mechanical structure of the device. Attractive force for wiggler magnets is much larger than that by an undulator, so conventional structures tend to be very rigid and heavy in order to avoid deflection. As NSLS-II DWs are presumed to be fixed-gap devices, no strict requirement for gap parallelness is required for the open position. One option is the scheme employed at the Source Development Laboratory at BNL, which utilizes inner and outer cages with roller bearings. Other possibilities will be considered.

References

[5.5.1.1] J. Safranek, et al., Nonlinear dynamics in a SPEAR wiggler, *Phys. Rev. ST*, Acc. and Beam, Vol. 5, p.010701 (2002).

5.5.2 Tunable Hard X-ray Sources

A decade ago, the hard x-ray region of the spectrum by undulators could only be covered at high-energy machines, such as ESRF, APS, and SPring-8. The advent of a mini-gap, short-period in-vacuum undulator, dubbed IVUN [5.5.1.1] in 1997 at the National Synchrotron Light Source has had a lasting impact on the design of synchrotron light source facilities all over the world. With the use of mini-gap, short-period undulators, a medium-energy ring (~3 GeV) can now produce tunable hard x-rays between 2 keV and 20 keV. Many years of successful operation of IVUs at SPring-8 [5.5.2.1], NSLS, and, more recently, at SLS and ESRF have demonstrated the reliability of IVUs. The NSLS currently has three IVUs in operation.

A long-standing concern in the ID community has been that the permanent magnets in small-gap IVUs would be gradually demagnetized and degraded by radiation, due to their proximity to the electron beam and exposure to synchrotron radiation. The conservative approach has been to use Sm_2Co_{17} magnets, rather than NdFeB magnets, because its lack of boron ought to make Sm_2Co_{17} more radiation resistant. However, after many years of successful operation at SPring-8, NSLS, and SLS without any signs of demagnetization, NdFeB IVUs with proper magnets having high intrinsic coercivity (H_{cj}) have proven to be quite radiation resistant. The newest high-remanence, high H_{cj} grades of NdFeB (such as NEOMAX AH series), developed for use in hybrid car motors, should be particularly robust and radiation resistant. We have used this high-temperature NdFeB in our most recent IVU and have based our PM ID designs for NSLS-II on this same magnet material.

Curiously, some out-of-vacuum undulators at APS have experienced localized demagnetization, particularly those with smaller aperture vacuum chambers. Detailed simulations and radiation measurements suggest that the main source of the demagnetizing radiation could be the tapered part of the aluminum vacuum chamber itself. Thus, out-of-vacuum IDs, such as the elliptically polarized undulators, may be more vulnerable to demagnetization than IVUs. Another contributing factor may be that the magnet grade used in APS undulators does not have particularly high enough H_{cj} and therefore does not withstand even localized radiation-induced heat.

Advantages of IVUs over fixed-chamber, out-of-vacuum IDs besides performance advantage are 1) that the former can be opened to provide a wide aperture during machine commissioning or beam studies, and 2) the lack of neutron-producing materials at transitions would mitigate magnet demagnetization.

A subject that needs further study is the impedance of the variable-gap IVUs. Earlier in this report, it was shown that the H-shaped space created by the gap space and the chamber forms a waveguide that contributes to transverse impedance. The RF transitions at the extremities of an ID must be properly tapered to reduce the geometric impedance. Modeling and RF measurements of real IVUs will be part of the design effort.

5.5.1 IVU (Baseline Device)

Room-temperature in-vacuum undulators are now considered to be a mature technology. Earlier concerns about demagnetization of permanent NdFeB magnets for IVUs are less of a concern now with proper magnet selection after many years of successful operation at SPring-8, NSLS, and SLS without any signs of demagnetization. The baseline design for a hard x-ray undulator for NSLS-II is based on a short-period linear undulator of the room temperature IVU type. This is the U20 device described in Chapter 5.

5.5.2 CPMU (Future Option)

For the future upgrade option, cryogenic permanent magnet undulator (CPMU) is considered. The enhancement is based on the fact that NdFeB magnet has a negative temperature coefficient of about –0.1%/K at 20°C for the remanent field (B_r), and also –0.5%/K for the intrinsic coercivity (H_{cj}). Therefore, one can expect higher field and higher radiation resistance simply by cooling the magnet array to lower temperature.

However, NdFeB exhibits a spin orientation below somewhere around 150K and its B_r starts decreasing as the temperature goes below this value [5.5.2.3]. An obvious advantage of operating NdFeB at the plateau around 150K (in addition to gaining 11 to 13% higher field), is greatly reduced sensitivity of the field to temperature gradients.

To test the effect of cooling NdFeB undulators, we measured our decommissioned 0.3 m Prototype Small-Gap Undulator in dry ice at –71°C, and demonstrated that the field increased as expected at –0.1%/°C, or about 9% when cooled down by ~90°C. However, this measurement did not reach the plateau in the B_r vs. temperature that is expected at around –120°C. Analysis of the Hall probe data showed no significant increase in phase error, or in trajectory error, except in the end terminations. We also measured a 10-pole 13.5 mm period PM-hybrid prototype in dry ice with similar results.

The SPring-8 and ESRF recently compared warm and cold measurements of a 1 - 2 m long CPMU. They found that while the fields increased as expected, magnetic field errors scaled and tracked with temperature as well. This suggests that a CPMU can be shimmed at room temperature, and it will remain optimized when it is cooled. This also supports the notion that a CPMU is inherently "fail-safe," in that it will still work well, albeit over a reduced tuning range, even if the cryocooling fails. If this result holds true for a hybrid CPMU, we will save an enormous amount of time in the magnetic shimming and spectral optimization of CPMUs by avoiding multiple cool-downs and warm-ups during the iterative shimming process. An important R&D task will be to verify by cold and warm measurements that field errors track with temperature in a hybrid CPMU as well.

5.5.2.1 "Cryo-Ready" MGU Installed in NSLS

NSLS has recently constructed and installed a 1 m long "cryo-ready" MGU for beamline X25 (18 mm period, B_y = 0.95 T at 5.6 mm gap) [5.5.2.4]. It has provision for cryogenic cooling by circulating cold He gas from a refrigerator through channels embedded in the magnet array platens. For the test we were able to cool it to 130K by circulating boil-off N_2 gas. This test demonstrated that the mechanical features designed to accommodate the large differential thermal contraction of the cold magnet arrays relative to the warm vacuum vessel worked. We mapped the undulator before and after thermal cycling and found no measurable magnetic changes.

5.5.2.2 Optical Gap Measurement

First-order gap control is performed using four external stepper motors with a linear encoder feedback system that positions each magnet girder to a mean reproducibility of 1 micron. The 1 m magnet length required multiple structural feed-throughs in the vacuum envelope to assure continuity between rigid external structural girders and the in-vacuum magnet girders. However, magnetic and mechanical measurements indicated that gap-dependent nonlinear magnetic forces, environmental temperature gradients, and operational conditions caused deflections of the in-vacuum magnet girders exceeding specifications. The external linear encoders could not measure these effects, and correction by the primary gap control system would be ineffective. The CPMU direct measurements of the magnet gap differed by greater than 1 mm with respect to the gap, as inferred by the external linear encoders. These measurements indicated that relying exclusively on a conventional external linear encoder-based control system is insufficient under extreme conditions, and a direct means of gap measurement and a secondary means of gap control are necessary to maintain micron control of the magnet girders over the full range of environmental and operational conditions. An LED-based system (e.g., Keyence LS-7030) that has a measurement accuracy of ±2 μm and repeatability of ±0.15 μm can be employed to provide a secondary means of gap control, to permit correction over the regime of these tertiary effects for up to 100 microns of nonlinear gap control. Very fine taper/bow control can be achieved by embedding temperature-controlled heaters for each post. This method successfully worked for the X25 MGU at NSLS. This feature is important even for RT-IVU to maintain very low phase errors. The effect of array deformation on phase error is examined in Section 5.5.2.4.

5.5.2.3 Optimizing the Device Design

Table 5.5.2.1 shows the possible combinations of period length, achievable peak field, and effective values of deflection parameter ($K_{y\ eff}$) at the undulator gap of 5 mm for a conventional room temperature IVU (20ºC) and cold (–120ºC) in-vacuum devices calculated by the same Radia [5.5.2.5] model used for the X25 MGU. These are all hybrid structures with vanadium permendur poles. Magnet type used in calculation for warm device is NEOMAX-32AH, Br =1.12T and Hcj =33kOe. This material was recently used for a similar device at Australian Light Source. Due to the much shorter beam lifetime and higher current for the NSLS-II storage ring than the NSLS x-ray ring, many more lost electrons will be produced as a demagnetization source. Therefore, more conservative material must be chosen compared to the NSLS MGUs. The magnet for cold type is NEOMAX-42AH Br =1.29T at 273K → 1.45T at 120K, and Hcj =24kOe at 273K → >40kOe at 120K. In this table, the effective K value for the non-sinusoidal field is calculated as

$$K_{x,y\ eff}{}^2 = 2\ \langle \gamma^2 \frac{v_{x,y}{}^2}{c^2} \rangle , \tag{5.5-1}$$

where *c* is the speed of light in vacuum, γ is the Lorentz factor, and *v* is the velocity of the electrons.

Table 5.5.2.1 Period-Length vs. Maximum Flux Density and Effective K Value for IVU at Room Temperature and 150K.

Period Length (mm)	Warm (B_r = 1.12 T) B_{peak} (T)	Warm K_{eff}	Cold (B_r = 1.45 T) B_{peak} (T)	Cold K_{eff}
16.0	0.76	1.11	0.98	1.43
17.5	1.87	1.37	1.11	1.74
19.0	0.97	1.63	1.21	2.03
20.0	1.03	1.81	1.26	2.22
21.0	1.10	1.99	1.31	2.40

All of the NSLS MGUs have severe limitations in their length. Therefore, the ideal magnetic termination at the extremities has to be compromised in order to increase the number of full-field-strength periods. Hybrid devices tend to have an inherently larger gap dependence of integrated field strength, due to the nonlinear characteristics of pole materials and anisotropy of permanent magnets. Various termination schemes that minimize the gap dependence for pure permanent magnet devices have been developed [5.7.9]. However, designs for hybrid devices have limited effectiveness. End effects tend to be less important for small-gap undulators than for large-gap, high-field wigglers.

5.5.2.4 Minimizing Phase Error

A critical requirement for short-period, in-vacuum MGUs in a medium-energy storage ring is retaining high spectral brightness, up to the 7th or even the 9th harmonic. Loss of spectral brightness is well correlated with optical phase error. Phase error can be defined as the cumulative path length difference between the electron's actual trajectory and an ideal trajectory, expressed in degrees of phase at the fundamental optical wavelength. Cumulative optical phase error of 2° RMS is considered state of the art and will be the target for all NSLS-II undulators. This is an especially challenging requirement for small-gap, short-period IDs, as shown below.

Phase error arises from three sources: 1) systematic gap error, 2) trajectory wander, and 3) random phase errors. We will next describe the techniques we have developed and use routinely to minimize phase error from these three sources.

Systematic phase error can be caused by a) bowing of the magnet arrays due to attractive magnetic forces, b) gap taper, and c) nonflatness of the magnet mounting surfaces. These are long-range gap variations, on the scale of many undulator periods, which cause a gradual variation of field amplitude, wiggle amplitude, and

therefore trajectory path length, without trajectory steering. To obtain a mechanical tolerance budget for these effects in the X25 MGU, we started with a finite-element analysis of an initial mechanical design for the magnet support beams, suspended on two hangers, under a distributed magnetic load of 8,000 N (due to the peak field of I T at a 5.6 mm gap). The resulting deflection profile was scaled to a field amplitude profile, which was numerically integrated to obtain the trajectory and, finally, a cumulative phase error profile. Figure 5.5.2.1 is a plot of the gap error (blue) and resulting cumulative phase error (magenta) vs. longitudinal position Z. The peak-to-valley deflection of 3 microns results in a RMS phase error of 0.75°. The figure shows that two supports per meter can induce a phase error of 0.75 degrees, due to deflection resulting from B = 1 T. Solid aluminum platens are assumed in this simulation.

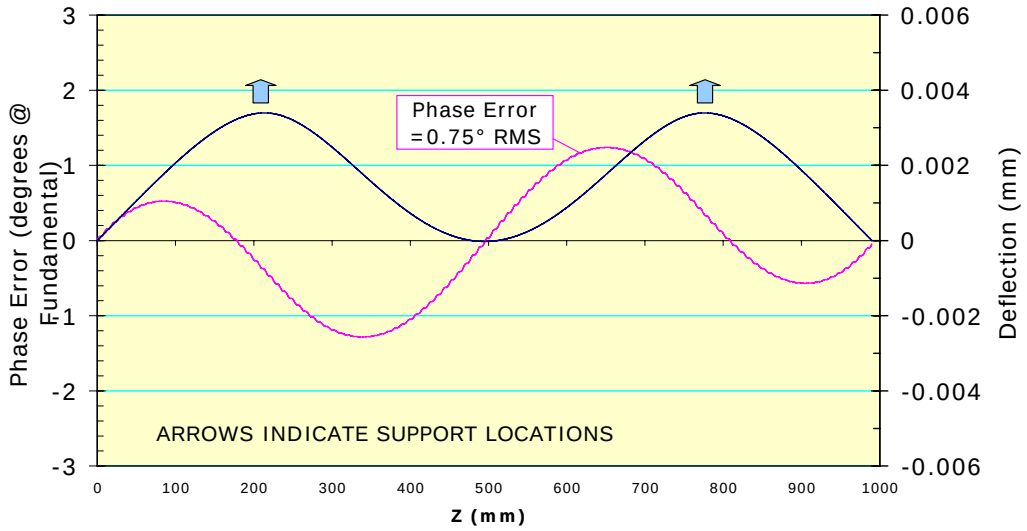

Figure 5.5.2.1 Phase error created by the mechanical deflection of aluminum magnet platens, due to the magnetic force of B = 1T.

The phase error created by 3.3 microns of linear tapering in 1 m is presented in Figure 5.5.2.2.

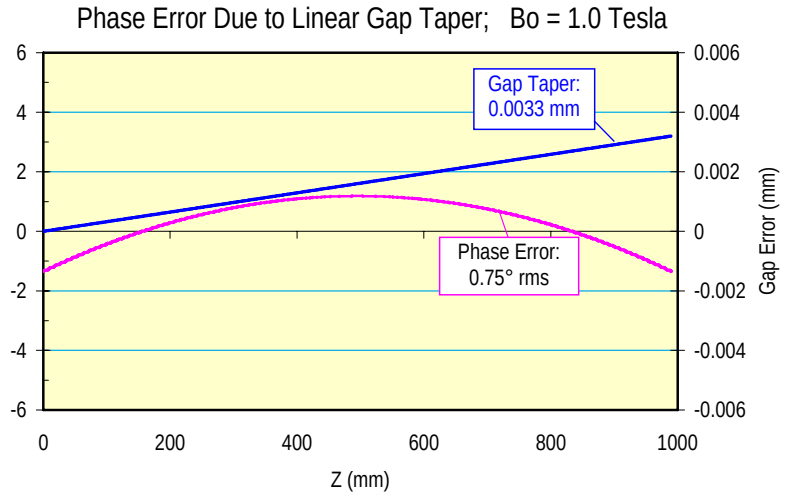

Figure 5.5.2.2 Phase error created by linear gap taper. B_0 = 1.0T.

Trajectory wander is caused by local, random field amplitude errors, which cause the trajectory to deviate from a straight line. The longer path is reflected in a phase error. Local steering errors can also accumulate over the length of the undulator as both integrated dipole (first integral error) and trajectory offset (second integral error). We routinely use the Pulsed Wire technique to quickly visualize the trajectory in undulators, identify the location and magnitude of steering errors, and apply steering shims to correct them. The pulsed

wire easily displays both the horizontal and vertical components of a trajectory, including the contribution of the Earth's field.

Random phase errors are nonsteering errors that remain following trajectory straightening and the removal of systematic phase errors. In a PM-hybrid undulator, random phase errors are mainly caused by variations in the strength of individual magnets, as well as by pole positioning errors. To minimize these, the individual magnets are first measured, then sorted, paired, selected, and assigned to specific locations in the arrays. Various manual and computer-aided sorting and selection algorithms have been developed and are considered standard practice.

Earth's field causes significant trajectory deflection in long undulators. The measured local Earth's field is about 0.4 Gauss with an inclination of about 14° from the vertical. The vertical component contributes an integrated (horizontally deflecting) dipole error of about 40 Gauss-cm/m. In a 3 m long CPMU, that adds up to a nontrivial dipole error of 120 Gauss-cm. The horizontal component is about 0.1 Gauss and oriented toward magnetic North. The effective (vertically deflecting) dipole error is <10 Gauss-cm/m and depends on the azimuthal orientation of the ID in the ring. The effect of Earth's field is readily visible on the pulsed wire as a parabolic trajectory component. It can be compensated by distributed trajectory shimming, or with external Helmholtz coils. In the X25 MGU we added a pair of 10-turn horizontal coils around the undulator vacuum vessel, powered by the end-pole trim supply from the old X25 wiggler previously residing at that location. Using the pulsed wire, we determined the optimal current to cancel Earth's field in the X25 MGU to be about 3.5 A. The small horizontal component was not compensated.

Other error specifications, such as maximum first and second integral and allowable integrated multipole requirements, will be specified before the engineering design phase.

5.5.2.5 Effect of Magnetic Field Errors on the Undulator Harmonics

The performance of real undulators is known to be poorer than the ideal case owing to magnetic field errors, despite valiant efforts to minimize such errors. It is generally accepted that the parameter which best relates magnetic field errors to spectral output is the RMS phase error ϕ. The RMS phase error ϕ is defined as the RMS path length difference between the real and ideal electron trajectories. It is calculated at the poles of the undulator and normalized to the wavelength of the fundamental harmonic (n = 1). (At higher harmonics (n >1), the RMS phase error is $n\phi$.) To date there has been no complete analytic treatment of the spectral effects of the phase errors. It has been argued that, for a zero-emittance electron beam, the relative on-axis brightness of the odd undulator harmonics n = 1, 3, 5, … emitted by an undulator with uncorrelated and Gaussian distributed phase errors is given by

$$B(n,\phi)/B(n,0) = e^{-n^2\phi^2} \tag{5.5.2-2}$$

where ϕ is the RMS phase error.

Recently, we have found empirically that this formula tends to underestimate the effect of phase errors for real undulators. For the two LCLS undulators discussed below, the expression above for a zero-emittance beam can be made to agree reasonably well with the result derived from magnetic measurements only if the RMS phase error is increased by ~20% from the measured value ($\phi \rightarrow 1.2\phi$). This is a large "correction" factor; more accurate results can be obtained by feeding the measured magnetic field profiles directly into undulator codes, such as UR or SPECTRA. Moreover, there is no analytical formula for phase error effects when the emittance needs to be taken into account, so we need to resort to numerical calculations.

Simulations were performed using measured magnetic field data from a set of undulators with RMS phase errors spanning a range from 2.0° to 3.7°. The measured magnetic field profiles and the storage ring parameters for NSLS-II were used as inputs to the undulator code UR in order to simulate realistic undulator spectral performance. If the results are a well-behaved function of phase error, one can then make a

determination of the maximum tolerable RMS phase error required to achieve a particular level of undulator spectral performance. As discussed below, the results confirm the intuition that achieving a 2° RMS phase error, or better, is important for maintaining high spectral brightness for the high NSLS-II harmonics (7, 9, and 11). These results also confirm the idea that the phase error effects become more significant as the ring emittance decreases.

5.5.2.5.1 Relative On-Axis Brightness for Harmonics 7, 9, and 11 vs. RMS Phase Errors for NSLS-II Undulators

Computer simulations of the relative on-axis brightness as a function of the RMS phase error were performed using the NSLS-II emittance and real measured magnetic fields of three undulators. Comparisons were made to the spectral performance of the same undulators with hypothetical ideal magnetic fields. The results are detailed below and show, for example, that the 9th harmonic undulator radiation degrades by about 15% if the RMS phase error increases from 2.0° to 3.0°.

Conditions

The NSLS-II storage ring parameters for a 5 m-long low-β insertion device straight section were used for these simulations. The following parameter values were used: emittances ε_h=0.55 nm, ε_v=0.01 nm, energy spread $\delta E/E$=0.1%, and β-functions β_h = 2.7 m, β_v=0.945 m. The resultant electron beam sizes and divergences are σ_h=38.5 μm, σ_v=3.1 μm, σ_h'=14.2 μrad, and σ_v'=3.2 μrad.

The following three undulators were studied:

- Linac Coherent Light Source undulator number 1 (LCLS #1), period length=3.0 cm, 113 periods; K and ϕ measured at 6.8 mm gap: K=3.50 and ϕ=3.54°
- Linac Coherent Light Source undulator number 2 (LCLS #2), period length=3.0 cm, 113 periods; K and ϕ measured at 6.8 mm gap: K=3.49 and ϕ=4.21°
- APS short undulator A (APS #40), K = 2.80, period length = 3.3 cm, 62 periods; K and ϕ measured at 10.5 mm gap: K = 2.80 and ϕ = 3.68°

Numerical calculations of the on-axis brightness for these three undulators were performed. In order to study the dependence on the RMS phase error, the LCLS undulator fields were scaled in both field strength (uniformly to a lower value) and period length to simulate a change of the RMS phase error (the RMS phase error decreases when the K value becomes smaller). Very minor adjustments to the on-axis view angle were applied, and as such, those fields represent real devices with true magnetic field errors. It is worth noting that for the LCLS undulators, the period length was scaled from 3.0 cm to 1.9 cm to simulate a shorter period-length undulator, such as the NSLS-II U19 CPMU hard x-ray undulator. This procedure allowed us to study undulators which have RMS phase errors covering the range 2.0° to 3.7°.

Results

The on-axis brightness of the 7th, 9th, and 11th harmonics, relative to the brightness of the corresponding harmonics of a hypothetical, ideal magnetic field undulator, is plotted in Figure 5.5.2.3 for the three undulators described above, simulated for their performance in the NSLS-II storage ring. The relative brightness of the 3rd and 5th harmonics is much closer to 100% and is not shown in this figure.

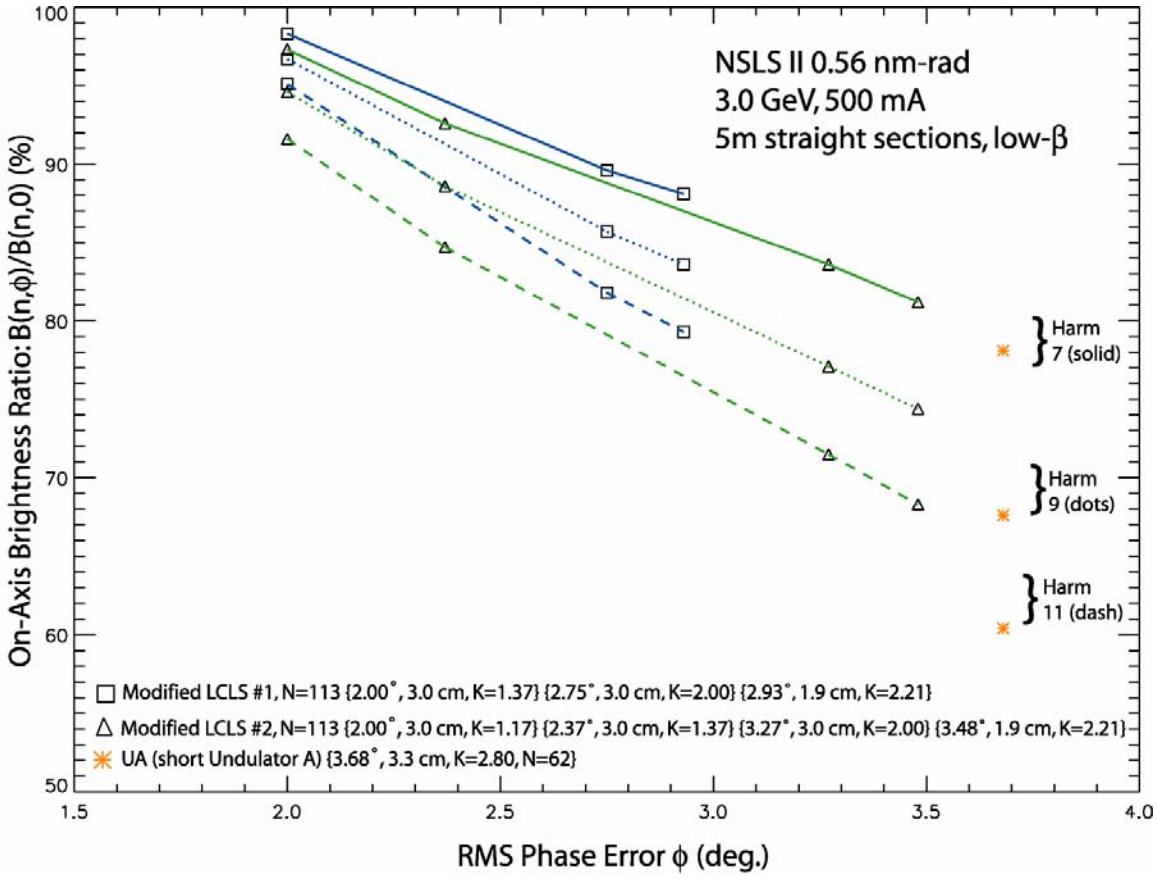

Figure 5.5.2.3 On-axis brightness of the 7th, 9th, and 11th harmonics of three undulators relative to the brightness of the corresponding harmonics of an ideal magnetic field undulator, as a function of the RMS phase error.

The key results of these simulations are as follows: improving the RMS phase error from 3.0° to 2.0° changes the relative brightness of the 7th harmonic from 86 to 98% (Δ_7 = 12% points), the 9th harmonic from 81 to 96% (Δ_9 = 15% points), and the 11th harmonic from 75 to 93% (Δ_{11} = 18% points).

Conclusions

The relative brightness of the NSLS-II undulator harmonics depends sensitively on the RMS phase error. The higher the harmonic number and the higher the RMS phase error, the faster is the rate of reduction. The rate of reduction is somewhat sensitive to the actual distribution of phase errors for real devices, but is much less sensitive to the actual K value or the undulator period length. For example, by improving the RMS phase error from 3.0° to 2.0°, the 9th harmonic would gain about 15%.

The effect of phase error becomes greater as the emittance of the storage ring decreases. For example, the performance drop for NSLS-II undulators would be 2 to 5% greater for harmonics 7–11 than for the same devices at APS, as a result of the smaller emittance of NSLS-II.

Future work on this subject should include simulations using the measured fields from recently built undulators around the world, including the 18 mm period undulator installed at NSLS beamline X25 in December 2005, which has a period length very close to the U19 CPMU proposed for NSLS-II and has a measured RMS phase error close to 2°.

5.5.2.6 Baseline IVU Magnetic Design

The base design for the NSLS-II hard x-ray planar device is derived from the NSLS cryo-ready undulator developed for X25. The X25 mini-gap in-vacuum undulator has an 18 mm period length, a minimum magnetic gap of 5.6 mm and length of 1 m, and is designed to be operated at 150 K. The NSLS-II U20 IVU will have a minimum gap of 5 mm and will be 3 m long, but most of its other requirements are similar to those for the X25 MGU. The main parameters are given in Table 5.5.2.1

Table 5.5.2.2 shows the expected mechanical tolerances of the magnetic arrays.

Table 5.5.2.2 Mechanical Tolerances.

Item	Tolerance
Magnet/pole width [μm]	±100
Magnet height [μm]	± 25
Magnet thickness [μm]	±25
Pole height [μm]	± 25
Pole thickness [μm]	± 10
Pole-to-pole flatness [μm]	±10
Period [μm]	±10
Magnet array pitch/yaw/roll (relative) [μrad]	± 25
Magnet array horizontal/vertical rack [μm]	± 5
Gap control [μm]	± 5
Gap repeatability [μm]	± 5

The phase error for the device is required to be less than two degree RMS. Slight tapering, platen bowing, and other factors must be carefully controlled to achieve this level of phase error. As mentioned above, a novel gap measurement system using a commercial, high-precision, LED-based optical micrometer was incorporated in the X25 MGU to back up the linear encoders and to correct for gap changes due to differential contraction during cryogenic operation. The system monitors the magnet gap optically through viewports at either end of the MGU, ensuring gap accuracy of ±2 μm.

Figure 5.5.2.4 shows an isometric rendering of the MGU magnet arrays by Radia. Blue magnets have identical size and two different sized magnets are shown in green. Pieces in magenta represent permendur poles.

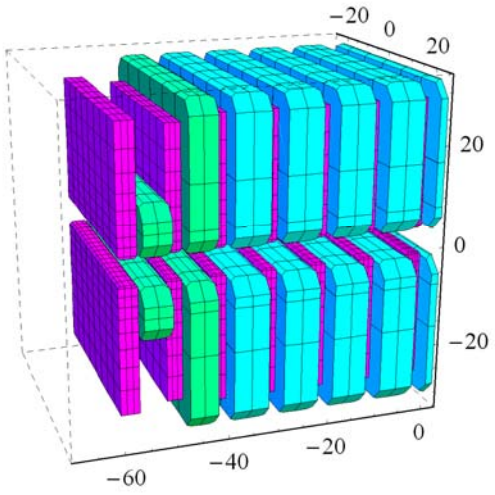

Figure 5.5.2.4 MGU magnet arrays. Only the first few periods are shown, for clarity. Units are millimeters.

The Radia simulations shown here were performed with a symmetrical model so the angular kick could be estimated. In the actual device we are likely to use an anti-symmetric structure to minimize the residual first integral. The values of magnet susceptibilities used are χ_m (para) = 0.02, χ_m (perp) = 0.42. The field and trajectory computed from the model are plotted in Figure 5.5.2.5 for gaps of a) 5.0 mm and b) 11.0 mm. The trajectory is calculated by a particle-tracking Runge-Kutta routine. The particle is launched with zero offset and angle (x = 0, x' = 0), and its position and angle are calculated every 0.53 mm (36 points per period). The gap dependence of the first integral is shown in Figure 5.5.2.6. The amount of change in the first integral found here can be easily compensated by external coils.

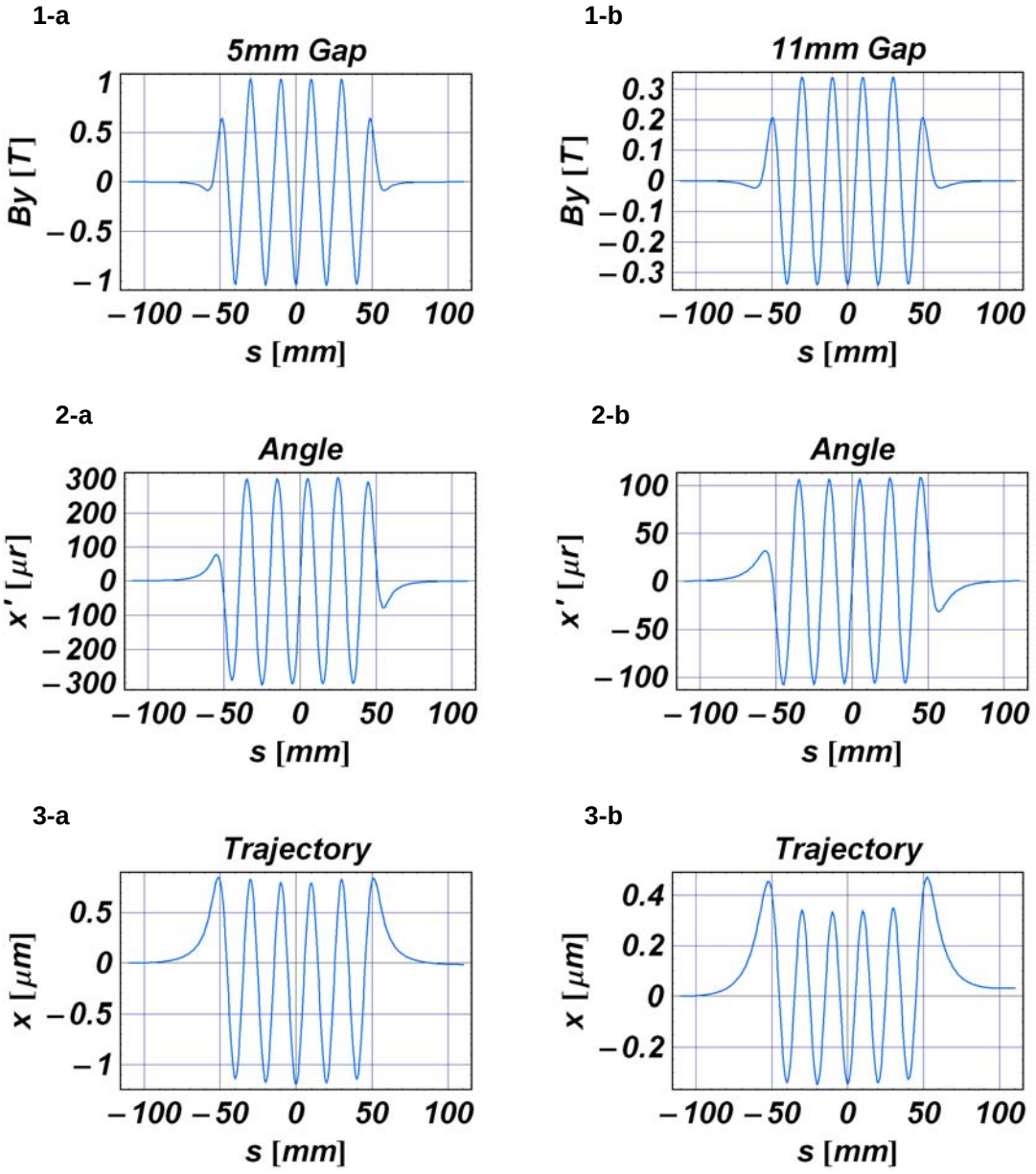

Figure 5.5.2.5 Gap dependence. Field, angle, and trajectory plots for the 7-period model for (column **a**) minimum gap (5.0 mm) and (column **b**) maximum operating gap (11.0 mm).

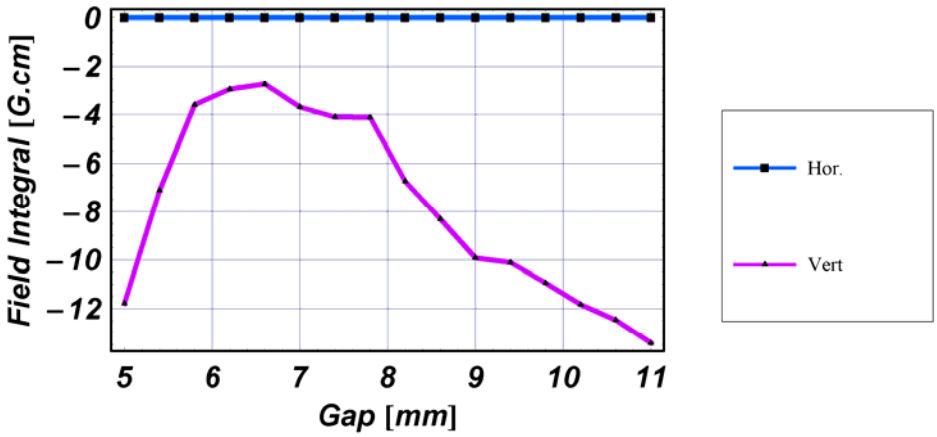

Figure 5.5.2.6 Gap dependence of the first integrals simulated for U20. Due to symmetric model structure, horizontal field integral dependence does not appear.

5.5.6 Vacuum and Mechanical Systems Development

A 3 m device will be constructed with three 1 m modules that are similar to the X25 MGU. The vacuum chamber is rectangular and opens along its length to facilitate magnetic field measurements and shimming. Most of the required vacuum components are mounted to this cover for easy access and for a cost-effective design. These components include ion pump/titanium sublimators, getter pumps, an RGA analyzer, a glow discharge cleaning system with associated pumping and view ports, an ion gauge, and bleed-up ports. The X25 system successfully achieved a pressure of less than 5×10^{-10} Torr, including magnets, after bakeout. The conceptual design in a CAD model is shown in Figure 5.5.2.7.

Techniques first demonstrated in the cryo-ready X25 MGU will be optimized and incorporated for the NSLS-II development program for the control system of the IVU. Systems such as an in-vacuum gap separation system will be modeled that can provide precision gap control with negligible effects from external temperature fluctuations and ultimately demonstrate a cost-effective alternative to more conventional gap separation and control systems.

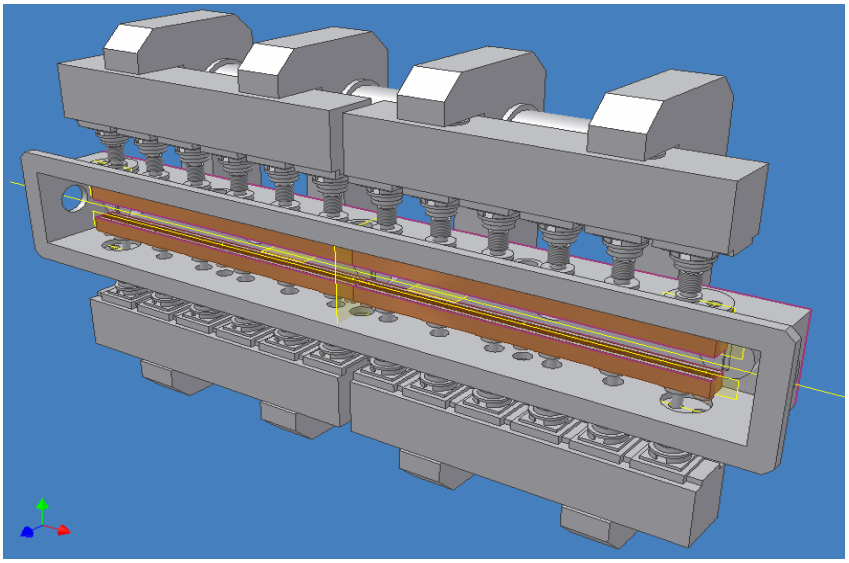

Figure 5.5.2.7 Conceptual design of U20.

References

[5.5.2.1] T. Tanabe, et al., "Development of an In-Vacuum Minipole Undulator Array for National Synchrotron Light Source In-Vacuum Undulator," *Rev. Sci. Instrum*. 69 (1), pp 18 – 24, (1998).

[5.5.2.2] H. Kitamura, "Recent development of insertion devices at SPring-8," *Nuc. Instr. & Meth. A* 467-468 (2001) p 110.

[5.5.2.3] M. Sagawa, et al., "Magnetic properties of rare-earth-iron-boron permanent materials," *J. Appl. Phys.* 57 (1985) pp 4094.

[5.5.2.4] T. Tanabe, et al., "X-25 cryo-ready in-vacuum undulator at the NSLS," AIP SRI2006 conference proceedings (to be published).

[5.5.2.5] O. Chubar, P. Elleaume, and J. Chavanne, *J. Sync. Rad*. 5, pp. 481–484 (1998).

5.5.3 Variable Polarization Device for Soft X-ray

The variable polarization undulator, also known as an elliptically polarized undulator, EPU, is becoming more popular, as its impact on beam dynamics can now be controlled to an acceptable level. Currently, no in-vacuum EPU has been constructed, because of the difficulty of having moving parts and a strong force in a UHV environment. Therefore, the baseline design for NSLS-II will be the permanent magnet out-of-vacuum EPU45 and EPU100 devices described in Section 5.1, but R&D may be carried out to investigate in-vacuum EPU designs.

Various schemes to generate variably polarized light from an insertion device have been proposed. An electromagnet-based design that switches the polarity cannot cover the required photon energy range (250 eV–2 keV). The most popular design, based on PM technology, is the Advanced Planar Polarized Light Emitter (APPLE) type [5.5.3.1]. It has been popular because it can generate all the possible polarization states with the minimum number of magnets. However, it also has a few deficiencies. Strong multipole components inherent to the design would reduce the dynamic aperture of the machine. This effect is due to the fact that horizontal field and vertical field are coupled, so static optimization for different gap and phase is difficult. In long-period devices, the electron's wiggle amplitude can be large enough for the field rolloff to affect the trajectory and result in a so-called "dynamic field integral," which is not measured by stretched wires or long coils. Recent efforts by various laboratories have mitigated these problems for limited types of operations [5.5.3.2].

There is an alternative design proposed for HiSOR by SPring-8 [5.5.3.3]. It separates the magnets for horizontal and vertical field, for ease of tuning as well as more moderate skew multipoles, at the expense of weaker achievable horizontal field. Detailed tracking studies will be carried out to decide which type of device is appropriate for NSLS-II.

Another concern for NSLS-II EPUs is the possible demagnetization of the permanent magnets by the use of the APS-style narrow gap vacuum chamber. Improvements to the vacuum chamber design will be investigated in order to minimize the source of radiation at the extremities of the chamber.

5.5.3.1 Anisotropy of Permanent Magnets

Rare-earth magnets used for insertion devices have permeability close to unity, so that, to first order, the magnetic induction from individual magnet blocks can be superposed to obtain the total field. However, more careful analysis shows that there is anisotropy in those magnets. The components of the permeability that are parallel to the preferred direction of magnetization (easy axis), and perpendicular to this direction, are different and lager than unity. The magnetic susceptibility χ_m and polarization J are defined as follows:

$$B = \mu H = \mu_0 \mu_r H = \mu_0 (\chi_m + 1) H , \quad (5.5.3\text{-}1)$$

$$J = \mu_0 \chi_m H \quad (5.5.3\text{-}2)$$

where B is magnetic induction, H is magnetic field strength, μ_0 the permeability of vacuum, and μ_r is the relative permeability defined for convenience.

The permeability can vary at different points on the hysteresis curve. For example, the value at the beginning of magnetization is termed initial permeability, and the largest gradient in the B-H curve is called maximum permeability. What is important in a magnetic circuit is the reversible or recoil permeability, which is the slope of a minor loop in the second quadrant. The recoil permeability is usually approximated by the slope of the major loop at H = 0. For NEOMAX 42AH, the susceptibility is estimated by the slope of the J-H curve around H = 0. The estimated values of susceptibilities from these curves are:

$$\chi_m \text{ (para)} = 0.02,\ \chi_m \text{ (perp)} = 0.42. \quad (5.5.3\text{-}3)$$

These values indicate that in the region where the magnetic flux lines deviate from the preferred direction of magnetization, the material can be nonlinear. For planar insertion devices, this region corresponds mostly to end sections, which determines the gap dependence of the field integral, in practical terms. However, in most EPUs, the field directions inside magnets vary greatly, depending on the array phase. For the CPMU these values will need to be measured at the operating temperature, in order to be more precise.

5.5.3.2 Advanced Options (Outside Baseline Project Scope)

In-vacuum EPU is still an R&D subject. The performance of any type of ID strongly depends on the available minimum magnetic gap. A 2.5 m long in-vacuum EPU may be developed in this program. BNL will assemble magnet and pole materials, develop in-vacuum gap separation and magnet module axial position actuators, and procure a vessel and undulator support system. Using the facilities in the Undulator Development Laboratory in Building 832, measurements and characterization of the EPU fields under various gaps and phases will be made, as well as field corrections. The in-vacuum EPU could then be installed for the X-1 beam line of NSLS I to verify performance prior to the move to NSLS-II. The goal of this development is to advance the state of the art in EPU technology, to demonstrate the first in-vacuum EPU, to resolve the uncertainty in the methods of measurement and shimming of EPUs to permit reliable and cost-effective operation, and to perfect a new class of insertion device, the in-vacuum EPU, that can be offered to meet the needs of NSLS-II users.

To switch the helicities at higher than 1 Hz, a tandem structure is needed so that light with opposite helicities is produced simultaneously for various switching schemes. In this case, each ID is located away from the center and the required beam stay-clear gap would increase. If a slower switching frequency is tolerated, one longer device with mechanical phase change is possible. Another possibility is to set up two helical undulators in tandem and have a phase shifter between them to change the resulting polarization [5.5.7.4]. In this case, two helical undulators can be in-vacuum type if limited tuning range can be tolerated. Table 5.5.3.1 shows the characteristics of an APPLE-II type EPU.

Table 5.5.3.1 Characteristics of an APPLE-II Type EPU. Assumed Br of the magnets is 1.35 T.

Period Length (mm)	Magnetic Gap (mm)	Helical ModePeak Field (Bx = By)	EffectiveKx / Ky	Linear ModeEffective Ky
40	6.5	0.87	3.2	4.87
42	8	0.77	3.0	4.76
45	10	0.68	2.87	4.67
45	11	0.62	2.6	4.38

5.3.3 EPU45 (APPLE-II) (Baseline Design)

One possibility is to install twin devices in an 8 m straight section. Assume that we can have a 5 mm vertical aperture for a 3 m device placed at the center of the 5 m straight, with vertical beta function equal to 1 m at the insertion center. In this case, the ring aperture (A) is:

$$A = \frac{gap}{\sqrt{\beta(end)}} = \frac{gap}{\sqrt{\beta_0 + (end)^2 / \beta_0}} = \frac{5mm}{\sqrt{(1+1.5^2)m}} = 2.77mm/\sqrt{m}\,. \quad (5.5.3\text{-}4)$$

We must verify that this is sufficient, but once we determine that this is acceptable, the required aperture y for an insertion device of length L placed at the center of a straight with beta-function β_0 at the center is determined to be

$$y = A\sqrt{\beta_0 + \frac{(L/2)^2}{\beta_0}} \tag{5.5.3-5}$$

For the 8 m straights β_0 = 3 m, we find the required vertical aperture is 7.4 mm at the half length of 3. 5 m. An 8 mm aperture chamber at APS allows 2.5 mm extra for the magnetic gap of their insertion device. Therefore, we will assume that the magnetic gap of the NSLS-II insertion device is close to 10 mm.

The minimum photon energy to be covered is 250 eV. An EPU45 with an APPLE-II type configuration shows the characteristics listed in Table 5.5.3.2. Here, the remanent fields of the NdFeB magnets are assumed to be 1.35 T.

Table 5.5.3.2 APPLE-II Type EPU45 Parameters.

Period length [mm]	45
Peak field (helical mode: v/h) [T]	0.68 / 0.68
Effective K	2.87
Minimum photon energy in helical mode [eV]	206
Minimum gap [mm]	10
Magnet horizontal size [mm]	50
Magnet vertical size [mm]	45
Remanent field (B_r) [T]	1.35

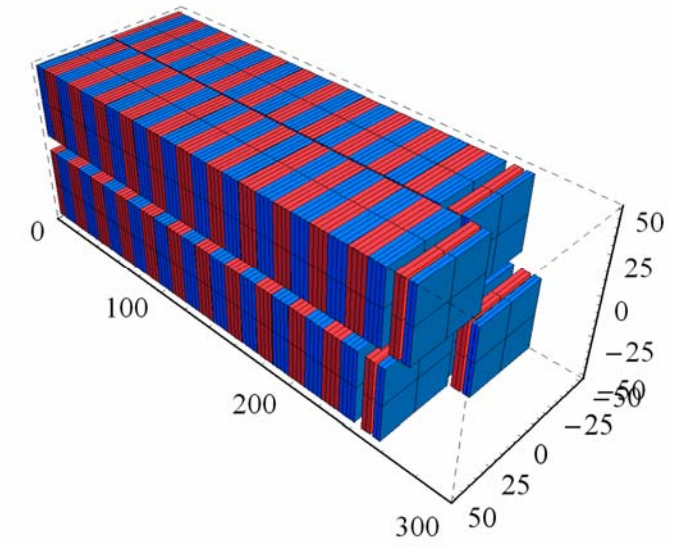

Figure 5.5.3.1 Magnet arrays of EPU45. Only the first few periods are shown for clarity. Units are millimeters. Vertically magnetized magnets are in red and horizontally magnetized magnets are in blue.

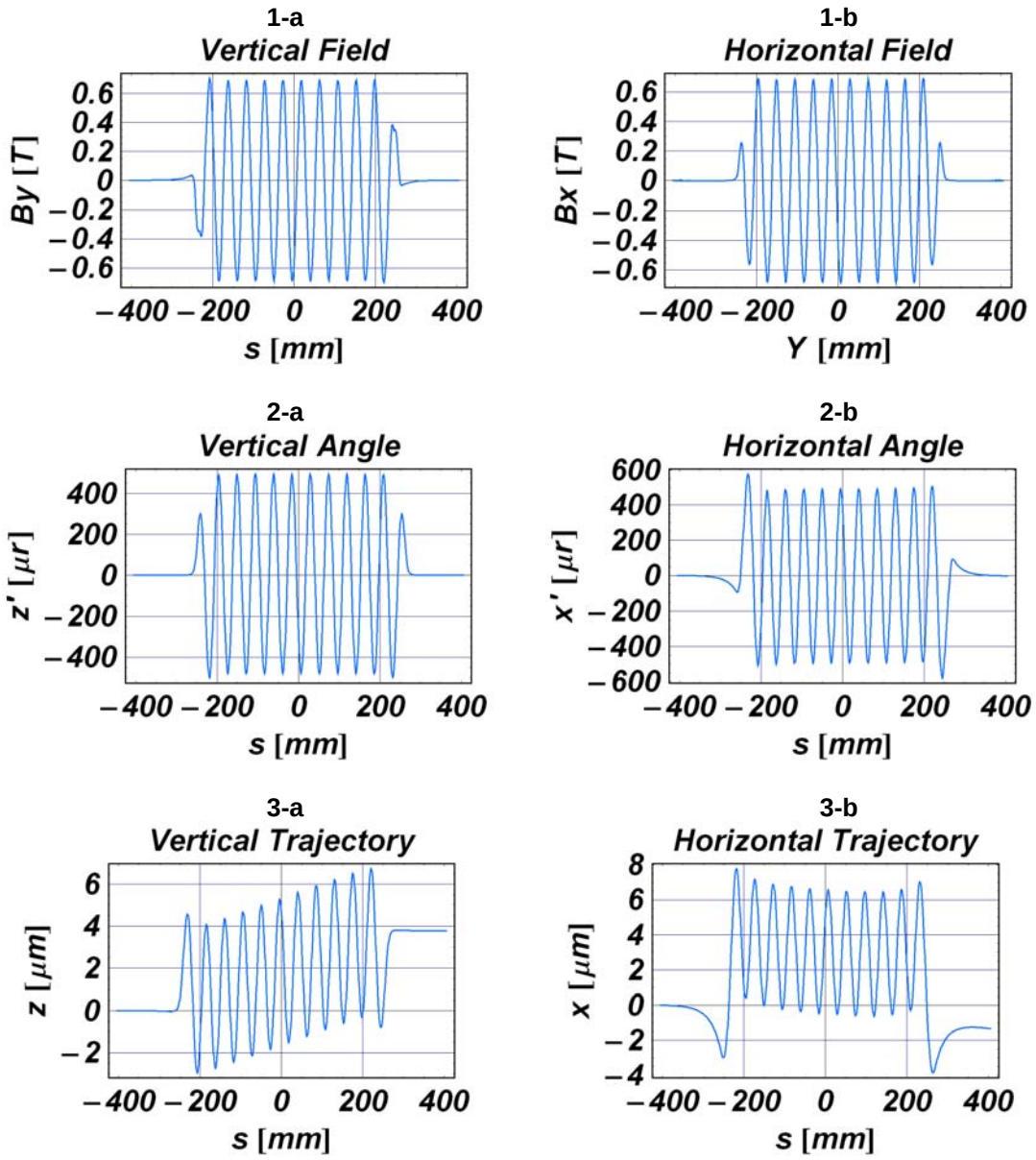

Figure 5.5.3.2 Field, angle and trajectory plots for the 11-period model of EPU45 in helical mode. **a)** vertical field, horizontal angle, horizontal trajectory and **b)** horizontal field, vertical angle, and vertical trajectory at a gap of 10 mm.

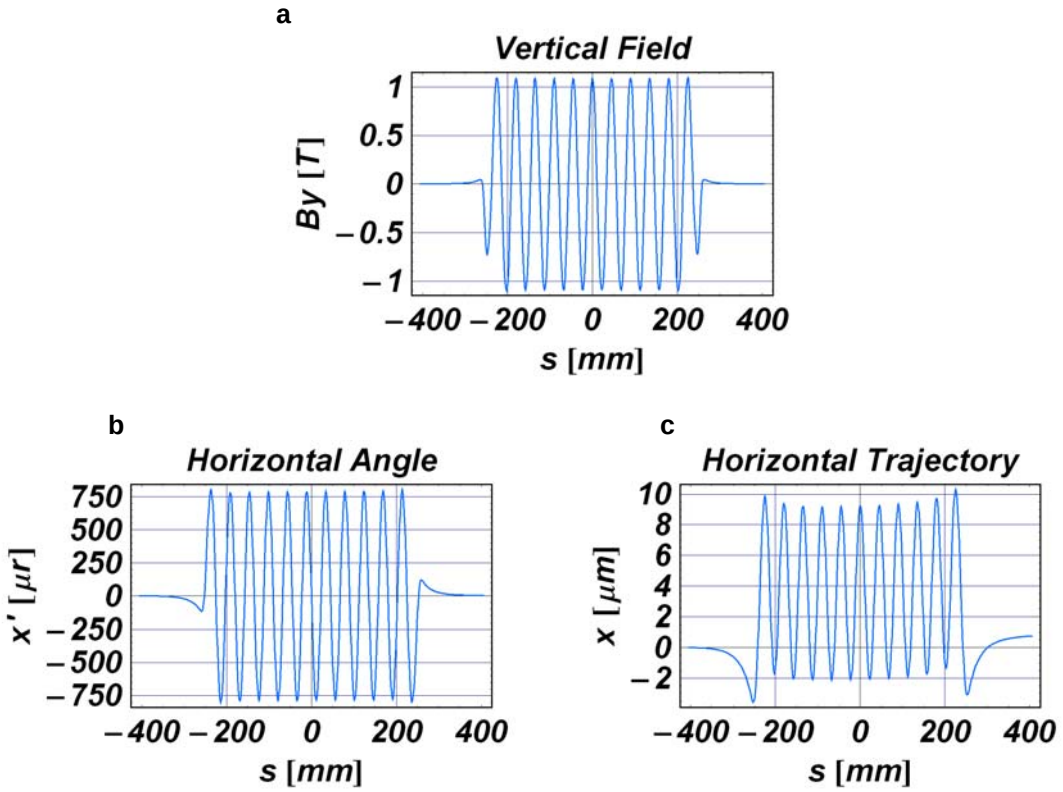

Figure 5.5.3.3 Field, angle, and trajectory plots for the 11-period model of EPU45 in linear mode. **a)** vertical field, **b)** horizontal angle, **c)** horizontal trajectory at a gap of 10 mm.

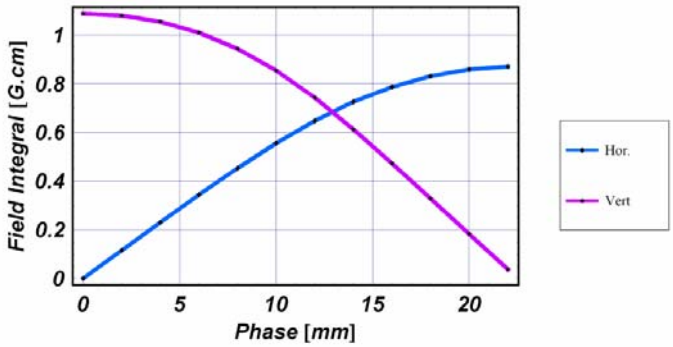

Figure 5.5.3.4 Fields vs. phase.

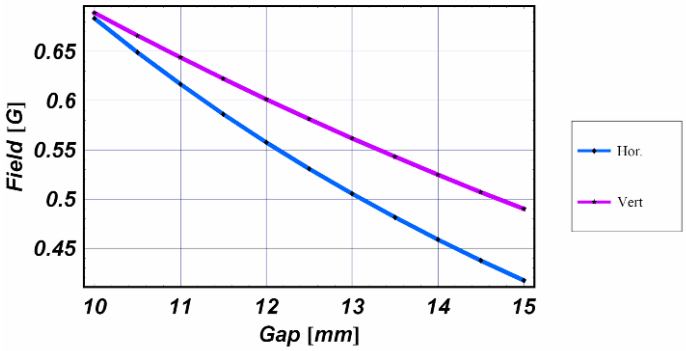

Figure 5.5.3.5 Fields vs. gap in helical mode.

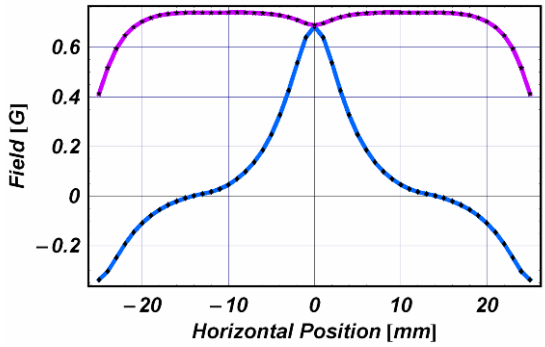

Figure 5.5.3.6 Fields vs. horizontal position at the origin in helical mode.

5.5.3.3.1. Mechanical Analysis

The small available transverse cross section of a device is also a concern for EPUs. Mechanical analyses have been conducted with slightly different parameters from EPU45. The chosen period length is 49 mm, and the minimum gap of 11 mm was selected due to cost and technical reasons. It was found that the maximum attractive force in gap direction is approximately 25000N, and that for phase direction is 15000N. The FEA analyses were done by Danfysik A/S as a part of the advanced conceptual design contract.

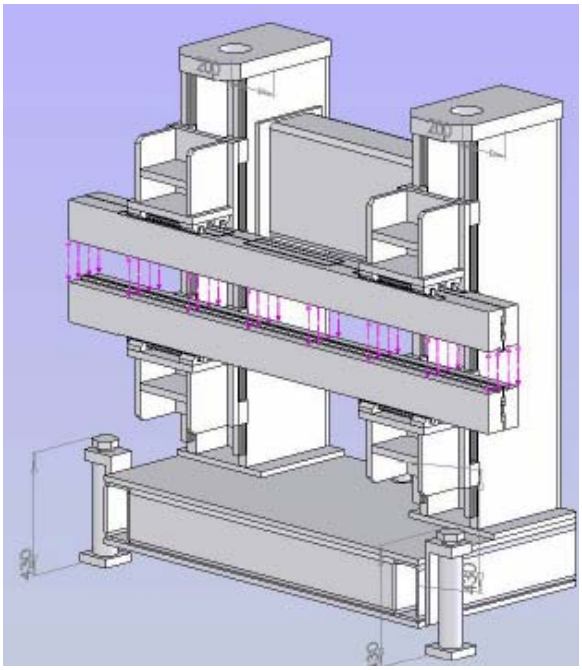

Figure 5.5.3.7 Applied force directions (magenta arrows).

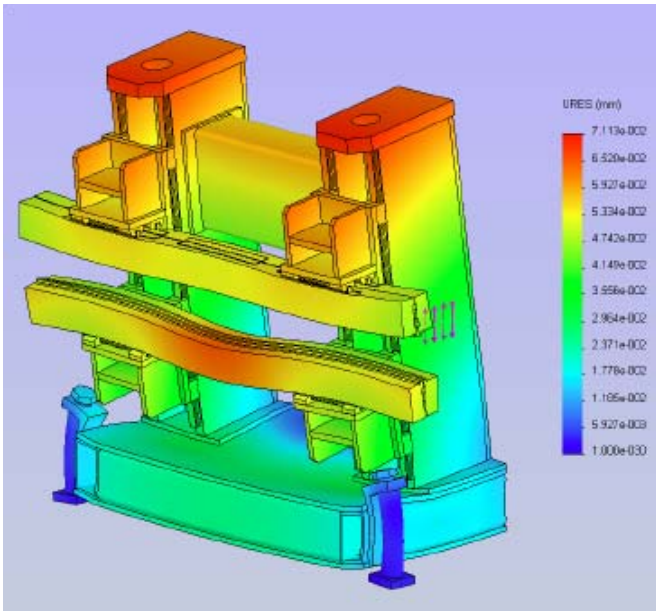

Figure 5.5.3.8 Displacement in vertical direction

Attractive force (12500N for each jaw and opposite directions)

The displacement plot shows that the maximum displacement is 0.071 mm at the top of the undulator, due to the weight of the motor and magnets. The maximum displacement between girders is approximately 0.013 mm. This amount will influence the achievable phase error in planar mode if one requires phase error better than 5 degrees, which is conventional for a commercially available Apple-II device.

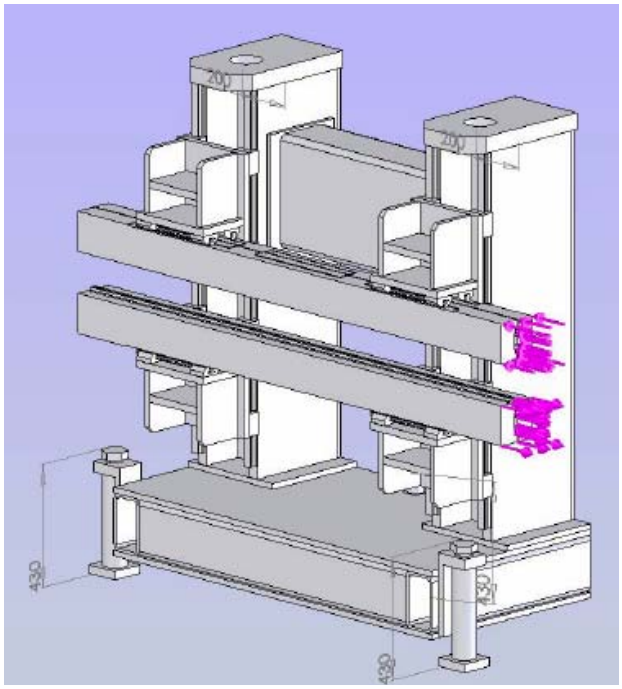

Figure 5.5.3.9 Applied force directions

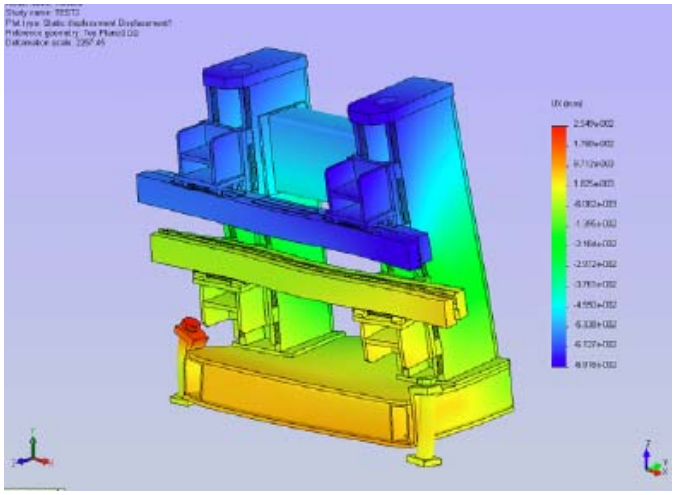

Figure 5.5.3.10 Displacement in longitudinal direction

Moment load (14700N per upper/lower jaw)

The maximum displacement in phase direction is found to be 0.062 mm. This amount can be easily compensated by the phase motion control.

5.5.3.4 EPU52 (HiSOR) Magnetic Design (Backup Option)

To alleviate a highly sharp horizontal field profile and the coupling of vertical and horizontal fields from the same magnet, a new design with three magnet arrays in each jaw has been proposed and implemented at UVSOR and HiSOR in Japan. Unlike the APPLE-II design, one array in the center produces vertical field and two arrays on the sides generate horizontal field. Therefore, each type can be separately shimmed to perfection upto lThe horizontal field profile is more benign than that from APPLE-II. The parameters for the HiSOR design are shown in Table 5.5.3.3, and a Radia drawing shows the design (Figure 5.5.3.11).

Table 5.5.3.3 HiSOR-Type EPU52 Parameters.

Period Length	52 mm
Peak Field (helical mode: v/h)	0.53 / 0.53T
Effective K	2.49
Minimum photon energy in helical mode	240 eV
Minimum gap	10 mm
Side Magnet Size (H/V)	50 / 45 mm
Center Magnet Width	14 mm
Remanent Field (Br)	1.35T

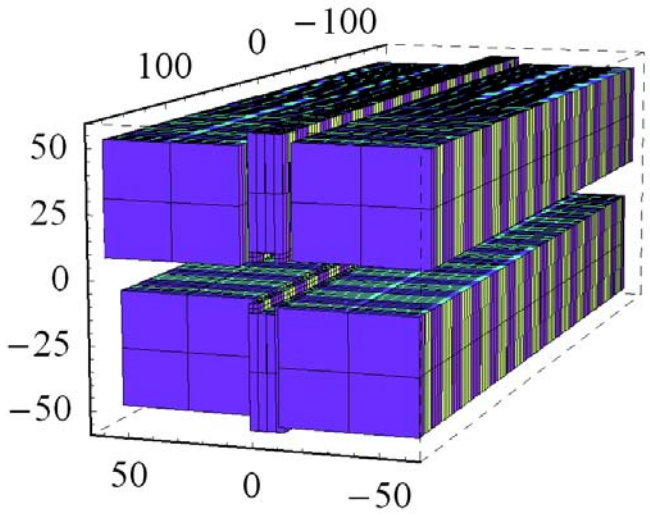

Figure 5.5.3.11 Magnet arrays of HiSOR-EPU52. Only the first few periods are shown, for clarity. Units are millimeters. Vertically magnetized magnets are in light green and horizontally magnetized magnets are in purple.

One disadvantage of the HiSOR design is that the maximum horizontal field is weaker than that of the APPLE-II for the same period length, due to the increased distance between the two arrays. Hence, slightly longer period length is required to obtain the same photon energy as with the APPLE-II design. If vertical linear polarization is needed, the vertical arrays can be shifted out of phase. However, some longitudinal components remain at the extremities, and tracking studies are needed to determine the detrimental effect.

The grooved-shape magnets in the center arrays improve the vertical field uniformity (Figure 5.5.3.13).

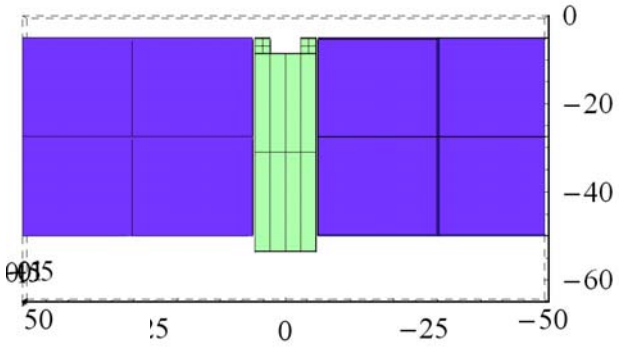

Figure 5.5.3.12 Cross-section of a magnetic array. Light green is for the vertical field and purple is for the horizontal.

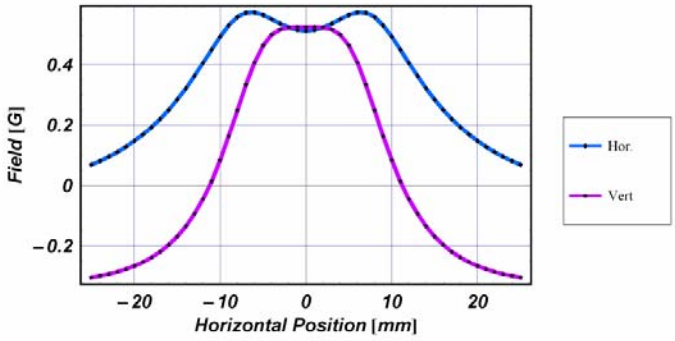

Figure 5.5.3.13 Field profile vs. horizontal position in helical mode.

References

[5.5.3.1] S. Sasaki , et al., "A new undulator generating variably polarized radiation," *Jpn. J. Appl. Phys*. 31 (1992) L1794.

[5.5.3.2] J. Bahrt, et al., "Preparing the BESSY APPLE-undulators for top-up operation," AIP SRI2006 conference proceedings (to be published).

[5.5.3.3] A. Hiraya, et al., "Undulator at HiSOR–A compact racetrack-type ring," *J. Sync. Rad.* (1998) 5, pp 445.

[5.5.3.4] T. Hara, et. al., "SPring-8 twin helical undulator," *J. Sync. Rad*. (1998) 5, pp426.

5.5.4 Three Pole Wiggler

5.5.4.1 Requirement

The NSLS-II three-pole wiggler (3PW) should be capable of producing the minimum of 2 mrad of fan angle above 1 T field. Field profile must be designed so as to minimize the emittance increase. Eq. (5.5.4.1) gives a rough estimate of emittance increase. ε_0 represents the initial emittance, N is the number of device, and B_w is the vertical field of the wiggler.

$$\varepsilon_w = \frac{\varepsilon_0 + 0.4\,N \int ds \left|B_w(s)\right|^3}{1 + 0.04\,N \int ds\, B_w(s)^2} \tag{5.5.4-1}$$

Figure 5.5.4.1 shows field, angle, and trajectory plots for the NSLS-II 3PW.

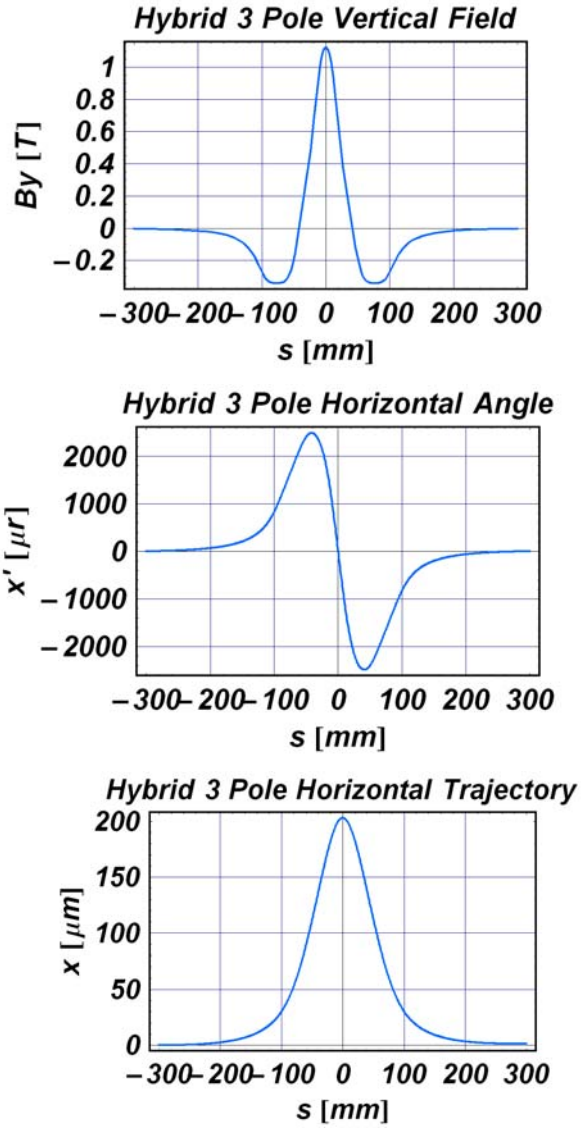

Figure 5.5.4.1 Field, angle, and trajectory plots for NSLS-II 3PW.

a) Vertical magnetic flux density at a gap of 12.5 mm

b) Horizontal angle at a gap of 12.5 mm

c) Horizontal trajectory at a gap of 12.5 mm

Figure 5.5.4.3 shows the preliminary magnetic structure of the 3PW and the distribution of magnetic flux density in the circuit. The magnetic gap in the center poles is 28 mm.

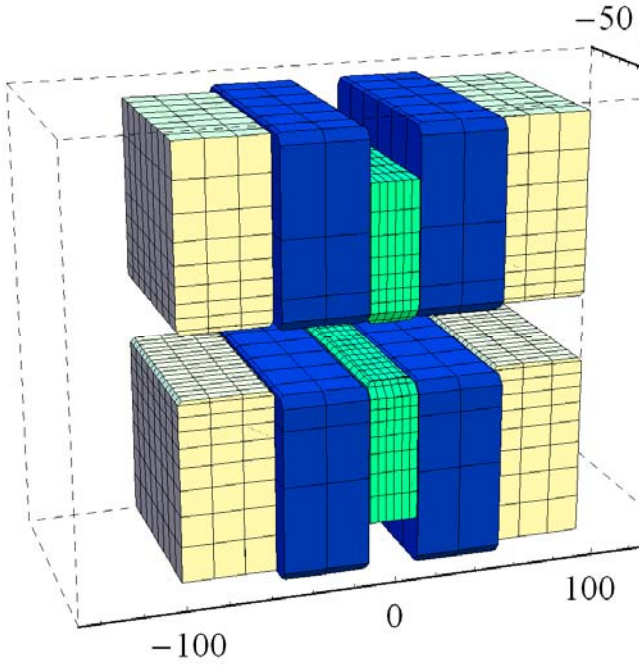

Figure 5.5.4.3 Magnetic structure of 3PW. Section in blue is NdFeB permanent magnet, green section is vanadium permendur and light yellow part is made of low-carbon steel.

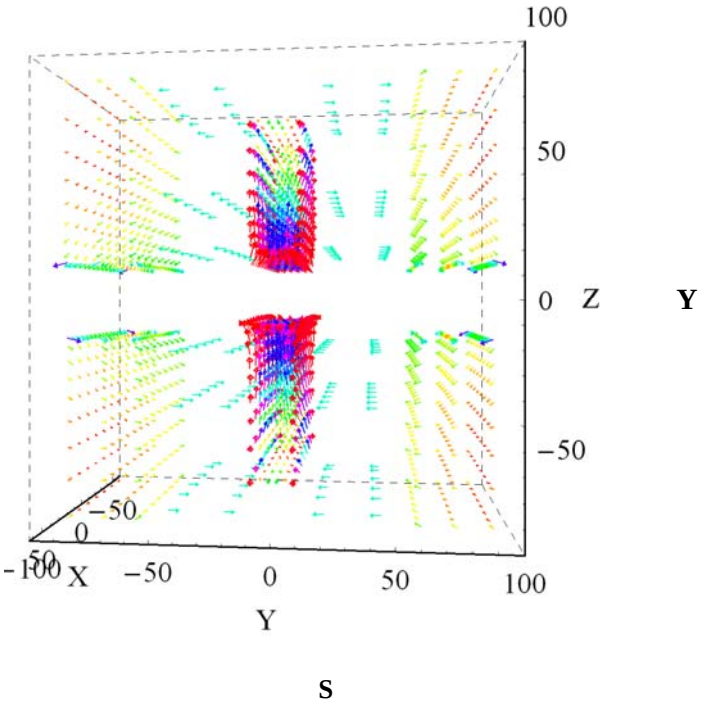

Figure 5.5.4.3 3PW magnetization vector plot.

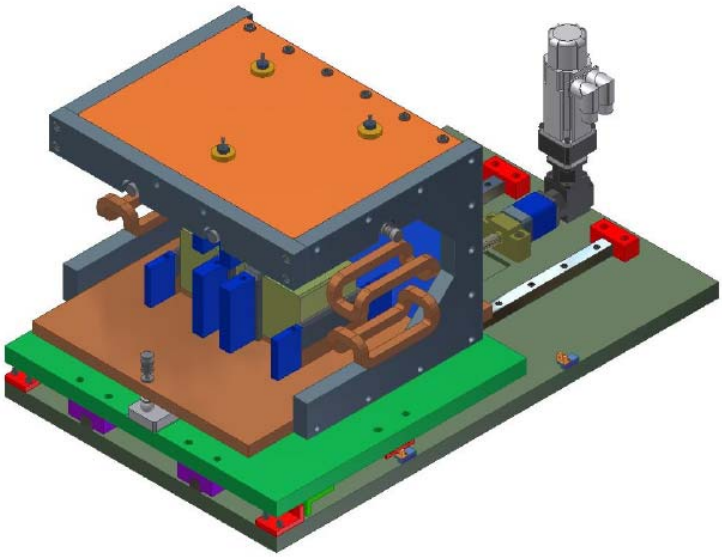

Figure 5.5.4.4
Isometric view of conceptual 3PW

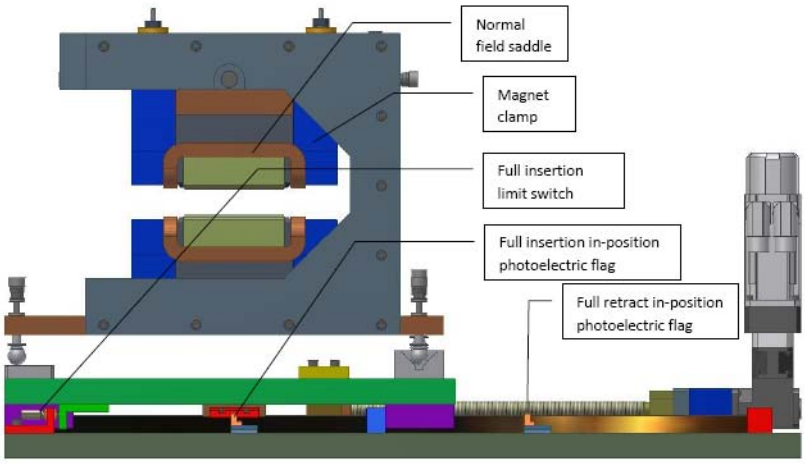

Figure 5.5.4.5
Side view of 3PW.

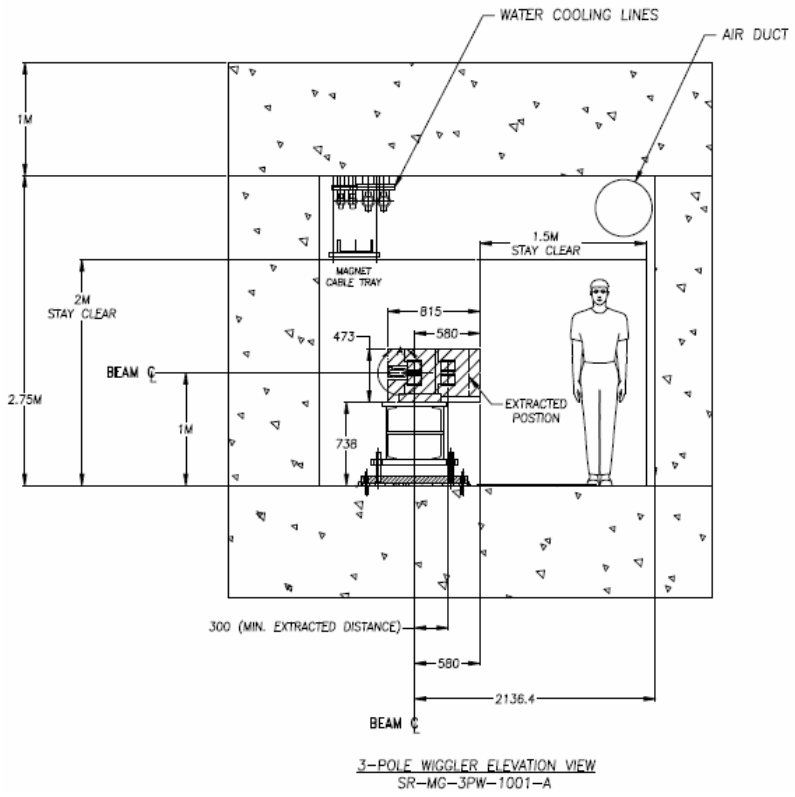

Figure 5.5.4.6 Tunnel cross section for 3PW location.

5.6 R&D Subjects and Insertion Devices for Future Consideration

In this section we briefly discuss three other types of insertion devices that will be explored in our R&D program. If these prove feasible, they would provide a number of benefits and will be considered for future installation at NSLS-II.

5.6.1 Magnetic Measurement Facility

Even though conventional insertion devices can be manufactured by industry, their ability to precisely measure the produced field is not in the state of art. Higher performance IDs to meet extremely high beam stability requirement must have very small field errors. Therefore it is essential that this project has its own insertion device magnetic measurement facility, in which each delivered device is certified and corrected if necessary. Due to handling of UHV components for IVUs, Class 10000 clean room with temperature controlled area must be secured for the measurement bench.

5.6.1.1 Requirements

Here are various requirements for the NSLS-II MMF:

1) clean area for insertion device assembly/staging
2) storage areas for insertion device parts and materials
3) temperature stabilized (± .2°C) clean-room (maybe class 10000) for magnetic survey, with gantry for overhead crane (twin 2-ton chain hoists), 7m Hall probe mapping bench, pulsed-wire test area, flowing water NMR for Hall probe calibration, and the associated electronic systems
4) machine shop, fully equipped, with storage for tooling
5) an area for winding superconducting insertion devices, with storage for parts
6) an area to setup and operate the Vertical Test Facility and also a Horizontal Test Facility for surveying superconducting insertion devices.
7) an area outside the main building—maybe an affixed structure--for bead blasting and polishing equipment, a hood for spraying paint, and an oven for curing coatings
8) office space with windows/emergency egress
9) an area for loading and unloading trucks

5.6.1.2 Building 832

Building 832 will be used to process, assemble, test and survey room temperature and cold permanent magnet undulators, and superconducting insertion devices and their associated hardware. Materials, supplies and magnet assemblies will be moved in and out of the building through the south-facing roll-up door. The large, 30 ton overhead crane will be used on occasion as required. Custom tooling/jigs for wire winding and special parts for the insertion devices and for the survey lab, will be fabricated in the shop. Parts will be polished and coated in the ‘affixed structure’ setup for that function. Areas will be set aside for the storage of permanent magnets, superconducting wire, basic hardware and other necessary ID parts and supplies. An area will be configured for winding superconducting insertion devices. In the back part of the high-bay area, the Vertical Test Facility, and later a Horizontal Test facility, will be setup for testing those superconducting designs. The permanent magnet type insertion devices will be assembled in the assembly/staging area. They will then be moved into the temperature stabilized clean-room for magnetic survey and field corrective

shimming. Cold measurement for CPMUs will also be conducted in this area. The finished devices will then be moved, maybe by flatbed trailer, to the ring for installation.

5.6.2 New Magnetic/Pole Materials

An avenue of further development of CPMUs is to investigate other rare-earth magnets that do not exhibit the spin re-orientation transition at 150K. For example, PrFeB has similar Br as NdFeB at room temperature, but its Br continues to increase further all the way down to 4K. PrFeB would permit use of liquid nitrogen to cool the CPMU to 77K and thereby attain an additional 5 to 7% increase in field. NEOMAX produced a few research samples of PrFeB several years ago, and again just recently. Although the material is not available commercially, we are discussing with NEOMAX and with SPring-8 the possibility of a funded PrFeB development project.

We will also investigate the use of exotic pole materials, such as oriented dysprosium, with a reported saturation flux density up to 3.5 Tesla at cryogenic temperatures. This opens the possibility of a CPMU built with PrFeB magnets and Dy poles, operating at 77K or lower with significantly higher performance than with NdFeB and permendur poles. This may ultimately reduce or eliminate the need for the complexity of superconducting undulators. This project will draw on the expertise in dysprosium and permanent magnet materials at the BNL Materials Science Department. If development of both PrFeB magnets and oriented Dy poles is successful, a short prototype undulator magnet module could be constructed and tested in our existing Superconducting Undulator Vertical Test Facility.

5.6.3 In-Vacuum Magnetic Measurement Systems

Two types of measurement systems are used to characterize the field quality of an insertion device at the magnetic measurement laboratory at NSLS. The first is a pulsed-wire measurement system that can be used to check the trajectories in both horizontal and vertical directions. It is also used to find the correct coil current of a Helmholz coil to cancel the earth field. The second type is a Hall probe mapping system. The Hall probe scan is done “on-the-fly,” starting from a precise home position, acquiring the desired number of samples per undulator period.

One of the challenges for CPMU development is to establish an accurate low-temperature field measurement system. For properly designed undulators, the differences in field quality between room temperature and low temperature are expected to be small. However, it is essential that the field quality be verified at the actual operating temperature. A vertically oriented cryogenic magnetic measurement apparatus for prototype undulator models up to 0.4 m in length has been developed and used at NSLS [5.6.1]. In order to measure full-length devices in a horizontal orientation, a new measurement scheme must be developed. The magnetic measurement should be done in the vacuum vessel at the cold operating temperature, but not necessarily in UHV. Figures 5.6.1 and 5.6.2 delineate the concept of an in-vacuum, in-situ Hall probe mapper based on square chamber design. It is mounted on the large rectangular front flange of the chamber. Hall probe position accuracy is maintained by a laser tracker and piezo controller. ESRF and SPring-8 have independently developed in-vacuum Hall probe mapper based on their cylindrical shape vacuum chamber. It is essential to establish our method of precise field measurement to produce the state of the art insertion device such as CPMU.

For field integral measurements, an in-vacuum moving wire system has already been developed by ACCEL and ESRF. A similar mechanism can be used for a pulsed-wire system.

There is no convenient way to make in-situ (i.e., in-vacuum) field error corrections unless a remote-control magnet adjustment mechanism is incorporated in the magnetic arrays. In the absence of this development, field error correction must be performed iteratively, where each iteration requires a lengthy series of warm-up, venting, measurement, adjustment, pump-down, and cool-down steps. Our goal is minimize the number of such iterations by 1) designing the mechanical components to minimize the

systematic field errors resulting from warm-up and cool-down, and 2) developing an efficient scheme of warm shimming and cold measurement. Ideally, field errors may track with temperature, so shimming at room temperature may suffice.

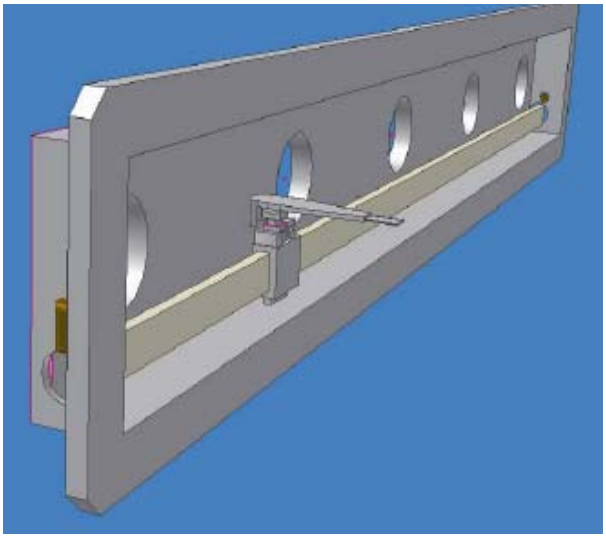

Figure 5.6.1 Hall probe mapper mounted on the flange cover.

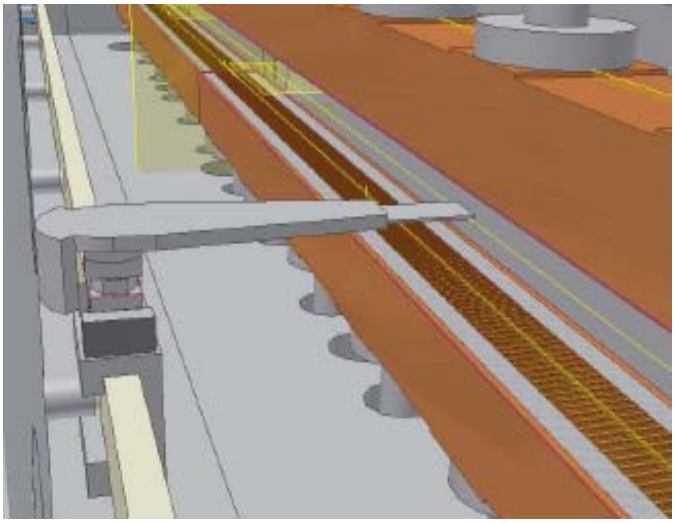

Figure 5.6.1 Mapper position with respect to the magnet arrays.

This system will be designed to be used primarily in the measurement laboratory but can also be used to perform in-situ measurements of insertion devices in remote locations such as a synchrotron tunnel. This system will incorporate a horizontal vacuum chamber that could accommodate either a CPMU or HTSCU that is 3+ m long and that demonstrates efficient installation of in-situ shimming and measurement of the magnet modules without the need for chamber reassembly. A cryogenic Hall probe, pulsed/vibrating wire, and moving wire will be investigated. The research phase will demonstrate the incorporation of an in-vacuum measuring system with the vacuum vessel and precision gap separation mechanisms.

The goal of this development is to demonstrate cryogenic undulator measurement concepts that will ultimately be used in the characterization, shimming, and in-situ measurements of all the production in-vacuum and cryogenic insertion devices.

5.6.4 Quasi-Periodic Undulator

Undulators designed to produce tunable vacuum ultra-violet and soft x-rays are of necessity long-period devices with period lengths of 40 to 100 mm or more. Because the characteristic K-parameter is proportional to the product of peak field and period, long-period undulators have necessarily high K values. Planar and elliptical undulators with high K-values produce spectra rich in harmonics (primarily odd-integer harmonics, since even harmonics are suppressed on-axis). In fact, the first few harmonics produced by high-K IDs have higher brightness and generate more SR power then the fundamental. If the user's monochromator is tuned to the fundamental, unwanted harmonics corresponding to higher orders of the monochromator pass through the exit slit unimpeded, polluting the monochromatic light and imposing an excessive heat load on optical components.

The Quasi-Periodic Undulator [5.6.2] was developed to overcome this problem. As the undulator's field amplitude pattern is altered, integer harmonics can be suppressed and replaced by noninteger harmonics. The latter do not coincide with higher orders of the monochromator and do not pass through the exit slit. The transmitted light is then purely monochromatic, and sensitive optics are protected. The monochromator must still absorb the unwanted harmonic power somewhere, but this can be accomplished by cooled absorbers at

the exit slit. As with a conventional undulator, the monochromator can be tuned to any of the noninteger harmonics of the QPU to extend the spectral coverage of the instrument.

The QPU concept has been applied to both planar and APPLE-II type IDs. In circular polarization mode, the APPLE-II generates only fundamental radiation on-axis, so the QPU is of no benefit in that case. But in planar and elliptical modes, the quasi-periodicity helps manage the harmonic power and improves spectral purity, as described above. Special care must be taken to absorb the radiated heat in vertical direction in helical / elliptical mode for long period device due to large value of K_x.

5.6.5 Superconducting Wiggler

Higher photon energies (above 20 keV) can be effectively covered by a superconducting wiggler at NSLS-II. For a field range of 3.5 T, 60 mm period length, and a 10 mm magnetic gap, low-temperature SCW technology is now well established. However, achieving 6.0 T with the same period and gap will be a challenging task. In contrast, devices based on the use of **h**igh-**t**emperature **s**uperconductors are a very promising approach for medium-field wigglers and would reduce the cost of both construction and operation. However, the current density now available for HTS wire remains inadequate to produce the necessary field. Thus, the baseline design for the NSLS-II SCW will be the SCW60 device described in Chapter 5, which is based on conventional LTS technology, but R&D will be carried out to investigate HTS wiggler designs.

5.6.6 Superconducting Undulator

The first superconducting undulator in an electron storage ring was installed at LURE, Orsay in 1979. Since then, various devices for FELs have been developed [5.6.3]. In the past fifteen years, IVUs have been the primary device for short-period undulators. One of the reasons for not using SCUs in the storage ring is the difficulty of opening the necessary gap for injection. A new SCU with a variable gap mechanism has been in operation at ANKA [5.6.4] for the past few years. It has a rather complicated two-vacuum vessel structure, one vacuum for UHV and the other for insulation. The vessels are separated by 300μm stainless steel foil. The required performance was barely achieved due to 1) excessive heat load, which reduced the critical current achievable, and 2) a structural problem that contributed to the degradation of phase errors.

SCUs with conventional NbTi wire face serious problems to reduce the heat load onto the device's cold mass to a level manageable with modern cryocoolers. Unfortunately, state-of-the-art cryocoolers have a cooling capacity of less than a few watts at 4K. What is needed is a different type of LTS wire that can withstand higher operating temperatures. One approach is to use Nb3Sn; this is being pursued by the ALS group [5.6.5]. This type of wire is best suited for high-field applications. However, it is difficult to create the precise structure required for undulators, due to the wind and react process. Another approach is to use APC NbTi wire, which is supposed to be operated at much higher current density than conventional NbTi wire. Using this approach, extra space for heat shielding may be available for a fixed-gap vacuum chamber.

Even with these developments, SCUs based on LTS technology will still have substantial thermal challenges. It may be that SCUs will not be viable until future developments in HTS technology make it possible to manufacture an HTS device. There is reason to be optimistic about this, and the NSLS-II project will monitor HTS industry developments.

Another issue for SCUs is field correction. Extra wiring to correct phase errors has been attempted, but distributed integrated multipole corrections appear to be difficult. They might require correction at the end of the device. These also are issues for future development.

The initial phase of this work was supported by two SCU-related LDRDs along with investigations to take advantage of new developments in the field of applied superconductivity.

One of the activities in this project is to demonstrate the capability for industry to produce lengths of APC NbTi and optimized Nb_3Sn superconductor that could be used to produce up to 1M long SCUs. Conductor

produced in this project can be used to produce 1/3 meter undulator prototype magnets that could be tested in the VTF.

In addition, this project will aggressively investigate films coated with high-temperature superconductors such as YBCO, MgB2, and other advanced materials, and determine the feasibility for their possible use in future SCUs and SCWs. Direct deposition methods for thick-film and multiple-layer superconducting for use in HTS magnet assemblies will be investigated in the first year. If feasible, these materials will be integrated into SCU shimming concept prototypes in the second year. This project will also investigate the design and demonstration of a superconducting EPU prototype that can be tested and measured in the VTF in year 2 or 3. The goal of this project is to demonstrate a variety of viable materials, manufacturing, and magnet design concepts for use in a NSLS-II SCU, and ultimately establish reliable superconducting insertion device technology that can be offered to meet the needs of NSLS-II users.

5.6.7 Revolver Type

If one type of magnetic array cannot satisfy the user's requirement, two or more different arrays could be used interchangeably, in a "revolver" type undulator system [5.6.6]. In-vacuum revolver type systems have also been developed. Revolver designs have been built at SPring-8 and ESRF and are operating reliably. In-vacuum revolver undulator was also developed by SPring-8 and installed at Pohang Light Source in Korea. This is a subject for future consideration, depending on the user requirements.

References

[5.6.1] D. Harder, et al., "Magnetic measurement system for the NSLS superconducting undulator vertical test facility," Proc. 2005 Particle Accelerator Conference, Knoxville, USA (2005).

[5.6.2] S. Sakaki, et al., "Conceptual design of quasiperiodic undulator," *Rev. Sci. Instrum*. 66 (2), p 1953 (1995).

[5.6.3] G. Ingold, et al., "Fabrication of a high-field short-period superconducting undulator," *Nuc. Instr. & Meth. A* 375 (1996) p. 451.

[5.6.4] A. Bernhard, et al., "Planar and Planar Helical Superconductive Undulators for Storage Rings: State of the art," Proc. 2004 European Particle Accelerator Conference, Lucerne (2004).

[5.6.5] S. Prestemon, et al., "Design and evaluation of a short period Nb3Sn superconducting undulator prototype," Proceed. 2003 Particle Accelerator Conference, Portland, U.S.A. p 1032 (2003).

[5.6.6] H. Kitamura, et al., "Recent developments of insertion devices at SPring-8," NIM-A, 467, (2001), pp 110.